# DESIGN AND CONSTRUCTION OF A FAST SPECTROMETER FOR FOURIER DOMAIN OPTICAL COHERENCE TOMOGRAPHY

by

MANISH KANKARIA

Presented to the Faculty of the Graduate School of

The University of Texas at Arlington and

The University of Texas Southwestern Medical Center at Dallas

in Partial Fulfillment of the Requirements

for the Degree of

MASTER OF SCIENCE IN BIOMEDICAL ENGINEERING

THE UNIVERSITY OF TEXAS AT ARLINGTON

May 2006

ACKNOWLEDGEMENTS

First and foremost, I would like to thank my parents for having sublime faith in me. You have always supported me in every decision of my life.

I would like to express my sincere gratitude to Dr. Digant Dave, whose guidance and ever present help cannot be overemphasized. You gave me a great opportunity to work on this project which helped me to develop my skills in the field of optical imaging.

To Dr. Khosrow Behbehani, Dr. Hanli Liu and Dr. J C Chiao, for imparting knowledge in me, in their field of expertise. Your advice and guidance helped me throughout the course of this project.

To my brothers, Deepak and Rajesh for being a great source of strength and support all though my life, without you none of this would have ever been possible.

I must thank my wife Mahika for her patience and understanding all though this work. Your love and encouragement has enabled me to complete this work.

My special thanks to Kapil for his indispensable technical assistance. I take this opportunity to thank all the members of Dr. Dave's group for their cooperation as and when required.

April 17, 2006

ABSTRACT

DESIGN AND CONSTRUCTION OF A FAST SPECTROMETER FOR FOURIER DOMAIN OPTICAL COHERENCE TOMOGRAPHY

Publication No. _____

Manish Kankaria, MS

The University of Texas at Arlington and
The University of Texas Southwestern Medical Center at Dallas, 2006

Supervising Professor: Dr. Digant Dave

A fast spectrometer capable of operating at 27.8 KHz is designed and calibrated to work in the wavelength range of 700-900 nm, to perform Fourier Domain Optical Coherence Tomography (FD-OCT). The OCT system is based on fiber-based Michelson's interferometer set up utilizing the spectrometer at the detector end. In FD-OCT system no reference scanning is necessary and hence images can be acquired at a much faster rate without any penalty to signal-to-noise ratio (SNR). A broadband Ti-sapphire source is used as input to the interferometer. Data at the rate of 60 MHz is

acquired from the spectrometer using a frame grabber and a DAQ card is used for synchronization and scanning of the galvanometers in the sample path. Lab-VIEW™ is used as interface for data collection and processing. The theoretical resolution of the spectrometer is calculated to be 0.11 nm resulting in the measurable depth range of 1.54 mm. Signal-to-noise for the system was experimentally found to be 52.05 dB. Video-rate OCT image acquisition capability of the FD-OCT system is demonstrated.

TABLE OF CONTENTS

Appendix

LIST OF ILLUSTRATIONS

LIST OF TABLES

Table Page

# CHAPTER 1

# INTRODUCTION

## 1.1 Background & Significance

Optical Coherence Tomography (OCT) is an interferometric imaging modality with a wide range of applications in the field of biomedical engineering [1]. It is used to provide high resolution cross-sectional tomographic images of highly scattering media. This technique is being explored for over a decade [2] to reveal the morphological structures of biological tissues and other samples. OCT employs a standard Michelson interferometer with a low coherence light source. In the interferometer the incoming beam is split into the reference path and the sample path which are recombined after back-reflection from their respective paths to form the interference signal. In a conventional time-domain OCT (TD-OCT) the reference mirror in the interferometer setup is rapidly scanned to provide a depth profile (A-Scan) within the sample. OCT image is then constructed by stacking several A-scans that are laterally displaced in a direction orthogonal to A-scan (B-Scan) [3,4, 5]. Later, Fourier Domain (FD-OCT) also known as spectral OCT was developed whereby the depth information could be obtained by measuring the spectral density at the detection arm of the interferometer with the help of a spectrometer [6, 7, 8, 9, 10]. The depth profile or A-scan is then obtained by taking the inverse FT of the spectral density obtained at the interferometer exit. The main advantage of FD-OCT system is that entire depth profile (A-scan) is

measured from a single spectrum with no mechanical scanning of the reference path. This permits faster acquisition of A-scans using a line scan CCD array. The use of a fast spectrometer has made video-rate imaging with this technique possible [11,12,13,14]. High speed acquisition of depth information without any moving parts minimizes any distortion in the OCT images due to motion of the sample. Further, in shot noise limit, the theoretical signal-to-noise ratio (SNR) of FD-OCT system is independent of the spectral bandwidth of light source. Thus, the axial resolution of the system, which is dependent on the bandwidth of the source, could be increased without any deterioration of SNR [15,16,17].

Higher resolution, non-invasive or minimally-invasive nature, and higher sensitivity has turned OCT into a highly promising technique for both in-vivo and ex-vivo biomedical applications. One of the most successful clinical applications of OCT has been in the field of ophthalmology. OCT can provide images revealing retinal pathology and can be used to diagnose and monitor several retinal diseases like glaucoma and macular edema [18,19]. OCT has also been used in gastroenterology for early diagnosis of tumors [20], and images delineating substructures of mucosa and submucosa in GI organs have been reported [21]. Dermatological applications of OCT have been demonstrated [22]. Research has also been carried out for the in-vivo applications with endoscopic and catheter based OCT techniques [22,23,24]. However the crucial limiting factor of OCT has been image acquisition speed. Development FD-OCT technique has led to overcome this limitation. Using FD-OCT 3-dimensional data sets can be rapidly acquired thus opening the possibility for comprehensive imaging.

Real-time imaging with video-rate acquisition speed has already been demonstrated for retinal applications [14].

## 1.2 Scope of this Thesis

The primary objective of this work was to construct a fast spectrometer and perform FD-OCT with video-rate acquisition speed.

The specific aims of this project are as follows:

*Aim 1:* Design and construction of a fast spectrometer for wavelength range of 700-900 nm and validate its reading with a standard spectrometer.

*Aim 2:* Integrate the fast spectrometer with the OCT setup to perform FD-OCT.

*Aim3:* Characterize the FD-OCT system and test its imaging capabilities with biological samples.

## 1.3 Organization of the Thesis

This thesis comprises of five chapters. This chapter presents a brief background and defines the scope of this work.

Chapter 2 consists of three sub-sections. The first section discuses the theory and mathematical framework of FD-OCT. The second section lays out the set up of the FD-OCT system. In the final section the spectrometer design and its calibration are presented.

Chapter 3 is subdivided into three sections. The first section discusses the spectrum acquisition process using the frame grabber and NI-IMAQ software interfacing. Data synchronization, processing and image construction utilizing the DAQ card, under LabVIEW™ environment for the FD-OCT system is discussed in section

two. In the final section of this chapter, system characterization of the FD-OCT system is explained.

Chapter 4 contains FD-OCT images of biological samples such as an onion and tissue. It also demonstrates the performance of the system at video-rate acquisition speed.

Chapter 5 lists out the overall performance and limitations of system. Future tasks are discussed including work towards implementing the system for real-time application.

CHAPTER 2

FD-OCT THEORY AND SYSTEM SETUP

## 2.1 Low Coherence Interferometry & FD-OCT

Optical Coherence Tomography is based on low coherence interferometry employing a Michelson's interferometer set up. A broad-band light source with short temporal coherence length [1] is used as an input to the interferometer. Figure 2.1 below shows a schematic diagram of a basic Michelson's interferometer setup.

In the interferometer setup shown in figure 2.1 the light from the broad-band light source is split up into the reference path and the sample path. The reference beam from reference path and the sample beam from the sample path are recombined at the

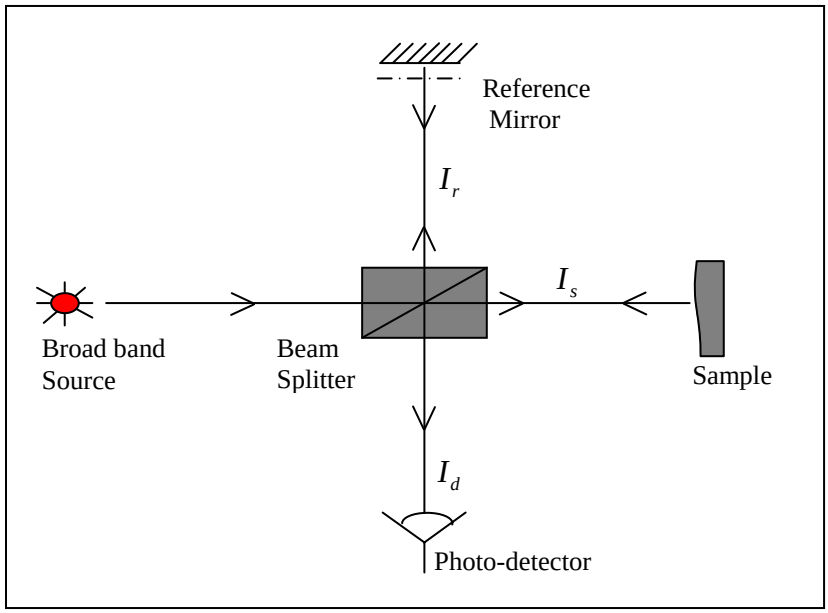


Figure 2.1: Michelson's interferometer setup

beam splitter after being reflected back from the reference and sample mirror respectively.

In TD-OCT, the photodetector detects the averaged intensity $I_d$, of the interference signal between the light reflected back from the reference path and the sample path. If $I_s$ and $I_r$ are sample and reference arm intensities respectively, $\tau$ is the delay associated with one of the beam traveling extra distance and $\Gamma(\tau)$ is the coherence function between the two waves then $I_d$ can be given as [26].

$$I_d = I_s + I_r + 2\sqrt{I_r I_s}\,2\,\mathrm{Re}\left[\Gamma(\tau)\right] \tag{2.1}$$

In TD-OCT the reference mirror is modulated to scan the optical path length to construct a single depth profile or A-scan. Closely spaced lateral depth scans are then obtained and stacked together to produce a single cross-sectional image of the sample.

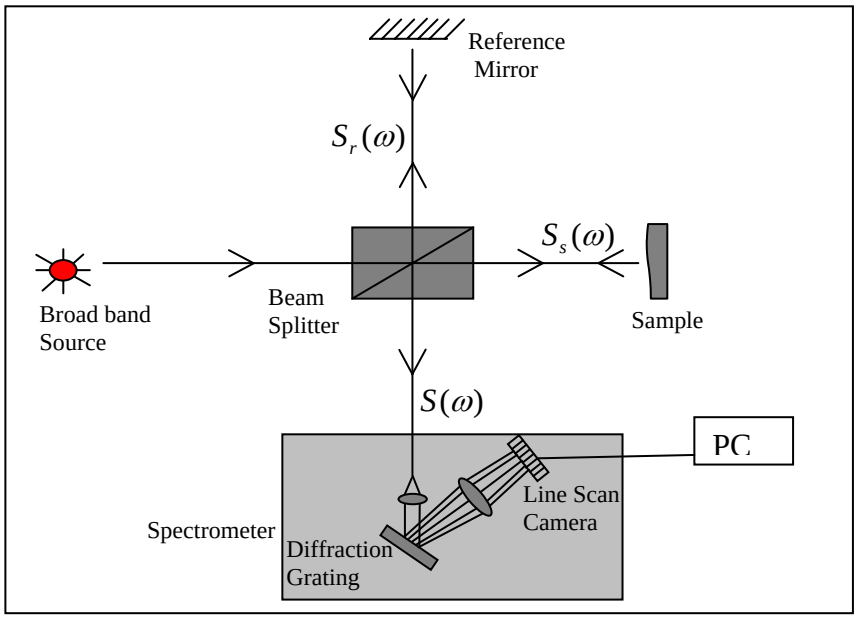


Figure 2.2: Michelson's interferometer setup for FD-OCT.

In FD-OCT system setup as shown in figure 2.2, the interference signal is detected by a spectrometer, where the interference beam is dispersed by a diffraction grating and individual wavelength components are detected by an array detector.

According to Wiener-Khintchine theorem spectral density $S(\omega)$ is related to coherence function $\Gamma(\tau)$ by expression

$$S(\omega) = \int_{-\infty}^{\infty} \Gamma(\tau) \exp(i\omega\tau) d\tau \qquad (2.2)$$

The coherence function $\Gamma(\tau)$ of a fluctuating optical field $U(t)$, considered at a time delay $\tau$, is given as

$$\Gamma(\tau) = \left\langle U^*(t) \cdot U(t+\tau) \right\rangle \qquad (2.3)$$

In the Michelson's interferometer set up shown in figure 2.2 the superposition of optical fields from the reference path and the sample path and can be written as

$$U(t) = k_r U(t - t_1) + k_s U(t - t_2) \qquad (2.4)$$

where $t_1$ and $t_2$ are the time taken by the light to traverse the reference arm and sample arm respectively. $k_r$ and $k_s$ are complex constants that represent the reflectivity of the objects in the reference and the sample arm. Thus, for the interferometer set up, the coherence function can be given by

$$\begin{aligned}\Gamma(\tau) = \left\langle U^*(t) \cdot U(t+\tau) \right\rangle = {} & k_r k_r^* \left\langle U^*(t-t_1) U(t+\tau-t_1) \right\rangle + k_s k_s^* \left\langle U^*(t-t_2) U(t+\tau-t_2) \right\rangle \\ & + k_r^* k_s \left\langle U^*(t-t_1) U(t+\tau-t_2) \right\rangle + k_s k_s^* \left\langle U^*(t-t_2) U(t+\tau-t_1) \right\rangle \end{aligned} \quad \ldots. \quad (2.5)$$

Since the optical fields are stationary we can shift the origin of time in all the

expressions on the right hand side of equation 2.5 and rewrite them as

$$\left\langle U^*(t-t_1)U(t+\tau-t_1)\right\rangle = \left\langle U^*(t)U(t+\tau)\right\rangle \tag{2.6}$$

$$\left\langle U^*(t-t_2)U(t+\tau-t_2)\right\rangle = \left\langle U^*(t)U(t+\tau)\right\rangle \tag{2.7}$$

$$\left\langle U^*(t-t_1)U(t+\tau-t_2)\right\rangle = \left\langle U^*(t)U(t+t_1-t_2+\tau)\right\rangle \tag{2.8}$$

$$\left\langle U^*(t-t_2)U(t+\tau-t_1)\right\rangle = \left\langle U^*(t)U(t+t_2-t_1+\tau)\right\rangle \tag{2.9}$$

Substituting 2.6, 2.7, 2.8 2.9 in equation 2.3 we can rewrite 2.5 as

$$\Gamma(\tau) = |k_r|^2\Gamma(\tau) + |k_S|^2\Gamma(\tau) + k_r^* k_S\Gamma(\tau+t_1-t_2) + k_r k_S^*\Gamma(\tau+t_2-t_1) \tag{2.10}$$

Further the Fourier transform (FT) of cross-correlation of two waves gives cross-spectral density function $G(\omega)$ given as follows

$$\int_{-\infty}^{\infty}\Gamma(\tau+t_1-t_2)\exp(i\omega\tau)d\tau = G(\omega)\exp\{-i\omega(t_1-t_2)\} \tag{2.11}$$

$$\int_{-\infty}^{\infty}\Gamma(\tau+t_2-t_1)\exp(i\omega\tau)d\tau = G(\omega)\exp\{i\omega(t_1-t_2)\} \tag{2.12}$$

Thus taking FT of equation 2.10 and substituting equation 2.2, 2.11 and 2.12 we have

$$S(\omega) = S_r(\omega) + S_s(\omega) + 2\,\mathrm{Re}\left[G(\omega)\exp(i\omega(t_1-t_2)\right] \tag{2.13}$$

where $S_r(\omega)$ and $S_s(\omega)$ are the spectral densities of reference and the sample arm respectively given as

$$S_r(\omega) = |k_r|^2 S(\omega) \quad \text{and} \quad S_s(\omega) = |k_s|^2 S(\omega) \tag{2.14}$$

Equation 2.13 can be expressed in terms of normalized cross-spectral density, also known as spectral degree of coherence as [30]

$$S(\omega) = S_r(\omega) + S_s(\omega) + 2\sqrt{S_r(\omega)} \cdot \sqrt{S_s(\omega)} \left|\mu_{sr}(\omega)\right| \cos\left[\beta_{rs}(\omega) - \delta\right] \quad (2.15)$$

where, the spectral degree of coherence is given by

$$\mu_{rs}(\omega) = \frac{G(\omega)}{\sqrt{S_r(\omega)} \cdot \sqrt{S_s(\omega)}} \quad (2.16)$$

and $\delta$ is defined as

$$\delta = (t_1 - t_2)\omega = \left(\frac{z_r - z_s}{c}\right)\omega = \frac{2\pi}{\lambda}(z_r - z_s) \quad (2.17)$$

$z_r$ and $z_s$ are the distances traveled in the reference and the sample arms respectively. $\lambda$ and $c$ are wavelength and speed of light respectively. In equation 2.15 $\beta_{rs}(\omega)$ is the argument of spectral degree of coherence.

In FD- OCT, the spectral density $S(\omega)$ is detected by a spectrometer where the interference beam is dispersed by a diffraction grating and individual wavelength components are detected by an array of detectors. The spectrum obtained from the spectrometer consists of three terms. $S_r(\omega)$ and $S_s(\omega)$ are the spectrum of light returning from the reference and the sample arm respectively. The third term is the interference term which contains the depth information. In the system setup, the path length in the sample and reference arm are made equal and only the optical pathlength mismatch resulting from the backscattering at various depths in the sample are encoded in the interference fringes in the spectrum.

From equation 2.15 and 2.17 it can be seen that the Fourier transformation of the interference spectrum would allow us to obtain depth resolved information of the sample. The spectrum acquired from the spectrometer measures intensity as a function

of wavelength λ. To reconstructs the axial scan or the scattering amplitude $a_s(z)$ of the sample as a function of depth *z*, the spectrum is evenly sampled in wavenumber *k* ($k = \frac{\omega}{c} = \frac{2\pi}{\lambda}$), which is the Fourier conjugate of z. If the amplitude of back reflected light from the reference arm is considered to be 1, then the interference signal I(*k*) in terms of wavenumber *k* can be given as [7]

$$I(k) = S(k)\left[1 + \frac{1}{2}F\left[a_s(z)\right] + \frac{1}{8}F\left[AC[a_s(z)]\right]\right] \tag{2.18}$$

where, S(*k*) is the spectral intensity distribution of the light source and AC represents auto-correlation arising from the interference within the sample itself. Inverse Fourier transform of equation 2.19 gives the convolution

$$F^{-1}\left[I(k)\right] = F^{-1}\left[S(k)\right] \otimes \left[\delta(z) + \frac{1}{2}a_s(z) + \frac{1}{8}AC\left[a_s(z)\right]\right] \tag{2.19}$$

From the IFT of the interference spectrum, $a_s(z)$ the scattering strength of the sample at different depths *z* , can be deduced.

In equation 2.19 the first convolution gives the FT of the source spectrum and gives rise to a constant dc offset. The second convolution encodes the information about the scattering amplitude $a_s(z)$. The third convolution contains autocorrelation terms which arise from the mutual interference within the scattering object. $a_s(z)$ is symmetric about *z* ,as *z* $\left(= |z_s - z_r|\right)$ is the absolute value of difference between sample and reference path. Thus if the sample is improperly positioned with respect to the reference plane, mirror (overlapping) images are seen.

*2.1.1. Depth Information in FD-OCT*

The depth information is encoded in the form of cosine function in the interference spectrum, which is revealed by taking the Fourier transformation of the interference signal I(*k*) (equation 2.19). As the distance $z$ between object and reference arm increases the modulation frequency in the spectrum increases. The spectrum acquired from spectrometer from the spectrometer is evenly sampled in *k* space by appropriate interpolation before taking the FT, to extract depth information. Figures 2.3 (a) and (c) show the interference spectrums when the sample is a mirror and placed at different depths. Figures 2.3 (b) and (d) are the FT of the spectrum after transforming from $\lambda$ to $k$ space, which indicates the corresponding depth.

If N is the number of pixels that are illuminated for total width $\Delta\lambda$ of the spectrum, by the spectrometer, with center wavelength $\lambda_0$, then the relation between the $i^{th}$ harmonic of the FT of spectrum and optical path length, z can be given by [8]

$$z_i = \frac{1}{2n}\frac{\lambda_0^2}{\Delta\lambda} i, \ 1< i <\text{N}/2 \tag{2.20}$$

where n is the refractive index of the object. According to the Nyquist criteria, the maximum measurable frequency and hence the depth is one half of the sample frequency of the photo diode array. Thus the maximum measurable depth, $\Delta z$ is

$$\Delta z = \frac{1}{4n}\frac{\lambda_0^2}{\Delta\lambda} N = \frac{1}{4n}\frac{\lambda_0^2}{\delta\lambda} \tag{2.21}$$

with $\delta\lambda$ being the resolution of the spectrometer.

*2.1.2. Resolution of FD-OCT*

In FD-OCT the achievable resolution will depend upon the coherence length of the

source. For a Gaussian spectrum coherence length can be given by [8]

$$l_c = \frac{4\ln 2}{\pi}\frac{\lambda_0^2}{\lambda_{FWHM}} \tag{2.22}$$

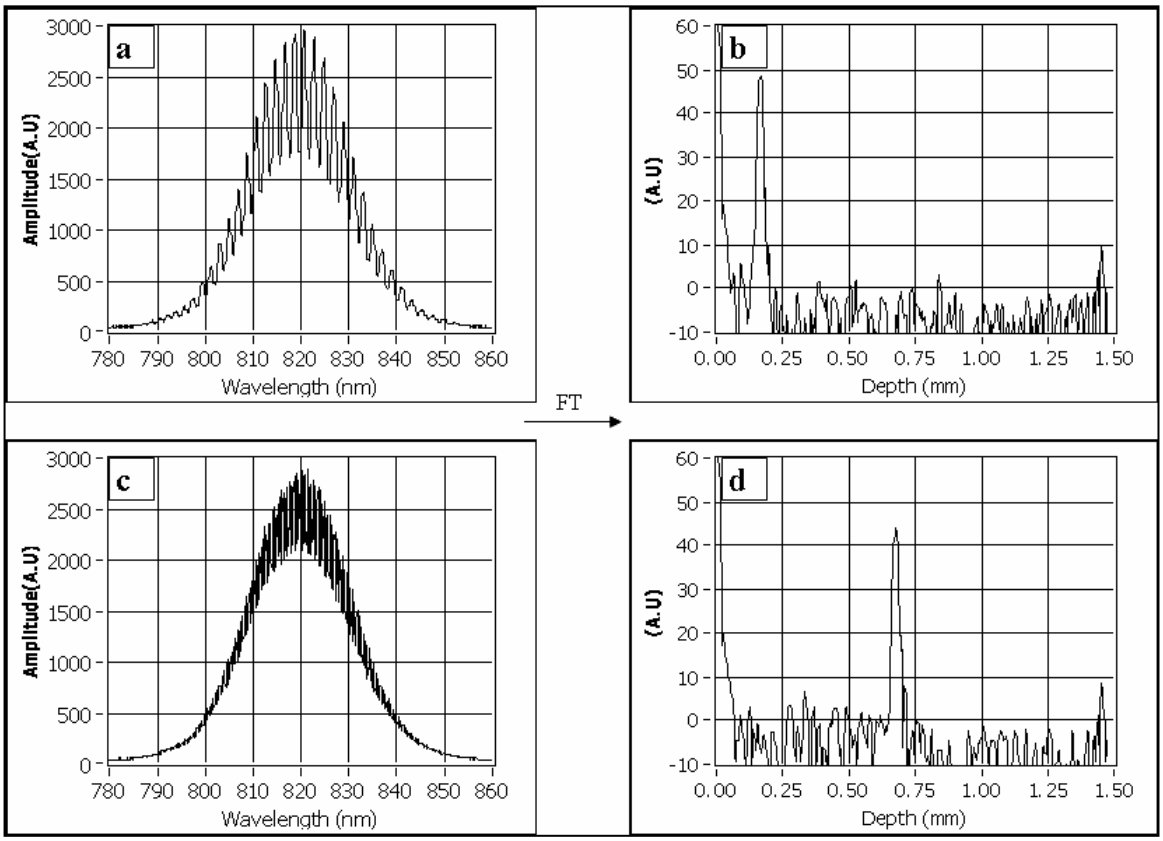


Figure 2.3: Interference signal and its Fourier Transform (FT) depicting depth information. Figures (a) and (c) shows the interference signal for different distances of sample mirror from reference plane. Figures (b) and (c) show their FT after converting from λ to k space.

In equation 2.22 FWHM implies full width at half maximum of the spectrum. The minimum resolvable distance or the axial resolution in a FD-OCT system is given as [8]

$$\delta z = \frac{l_c}{2n} = \frac{2\ln 2}{n\pi}\frac{\lambda_0^2}{\lambda_{FWHM}} \tag{2.23}$$

where, n is the refractive index of the medium. However for 2.23 to hold true, dispersion in the sample and the reference path must be matched. Under this condition a

broader spectrum would imply a shorter coherence length and hence give a higher resolution.

The transverse resolution of OCT system depends on the beam waist $\Delta x$ on the sample. For a gaussian beam, the beam waist on the sample is related to the numerical aperture, $n_a$, of the lens that focuses the beam on the sample and the mean-wavelength $\lambda$ by the following relation [25]

$$\Delta x = \frac{2\lambda}{\pi . n_a} = \frac{4\lambda}{\pi}\frac{f}{d} \tag{2.24}$$

where, $f$ is the focal length of the objective and $d$ is the beam diameter at the lens. The depth of focus (DOF) $b$ is given as

$$b = \frac{\pi\left(\Delta x^2\right)}{2\lambda} \tag{2.25}$$

Figure 2.4 shows the DOF and beam waist for a Gaussian beam.

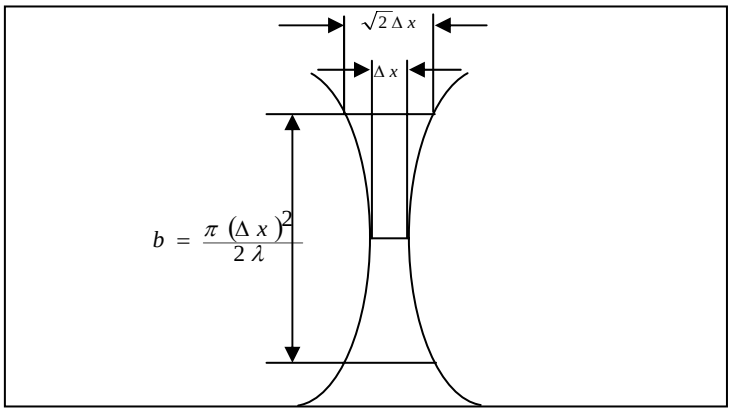


Figure 2.4: Illustration of depth of focus and beam waist.

A higher $n_a$ objective would provide a higher transverse resolution at the focus at the cost of smaller DOF and vice versa.

## 2.2 FD-OCT System Setup

A schematic diagram illustrating the set up of our fiber based Spectral OCT system is shown in figure 2.5. The output of the broad band light source is split into equal ratio between reference and the sample path using a 50:50 fiber coupler. The reference arm consists of a dispersion delay management line and in the sample arm a XY scanner is utilized for scanning the sample [26]. The interference spectrum of the light collected from both the arms is then fed to a fast spectrometer. A brief description of each of the component is as follows:

The input to the interferometer is a broadband Ti-Sapphire laser (Kapteyn-Murnane Laboratories, Boulder, CO) source capable of lasing in the wavelength range of 700-900 nm. The output spectrum of the source could be varied using a software interface provided by the laser manufacturer. A green laser with center wavelength of 532 nm is used to pump this source. The high output power ($\approx$400 mW) was attenuated using neutral density filters and coupled into fiber coupler using a beam coupling assembly. A 50:50 fiber coupler assembly (Canadian Instrumentation & Research Ltd.) formed the interferometer. Four arms of the interferometer consisted of SM750 fiber with a mode field diameter of 5.9 $\mu m$. Angle polished fiber connectors (FC/APC) were used to prevent any back reflection of light at the connector end into the interferometer.

The reference path consisted of a dispersion delay management line. In this set up light from the collimator is diffracted into its wavelength components with the help of a grating, and then focused on the mirror using an achromatic lens. The back-reflected light from the mirror combines at the grating after passing through the lens and

is collimated. This collimated beam is then diverted onto another mirror and allowed to retrace its path back into the collimator. The distance between the lens and the mirror was kept exactly one focal length. The lens and mirror assembly were put together on a linear stage. This arrangement allowed us to change the grating to lens distance to compensate for dispersion mismatch between the sample and the reference arm.

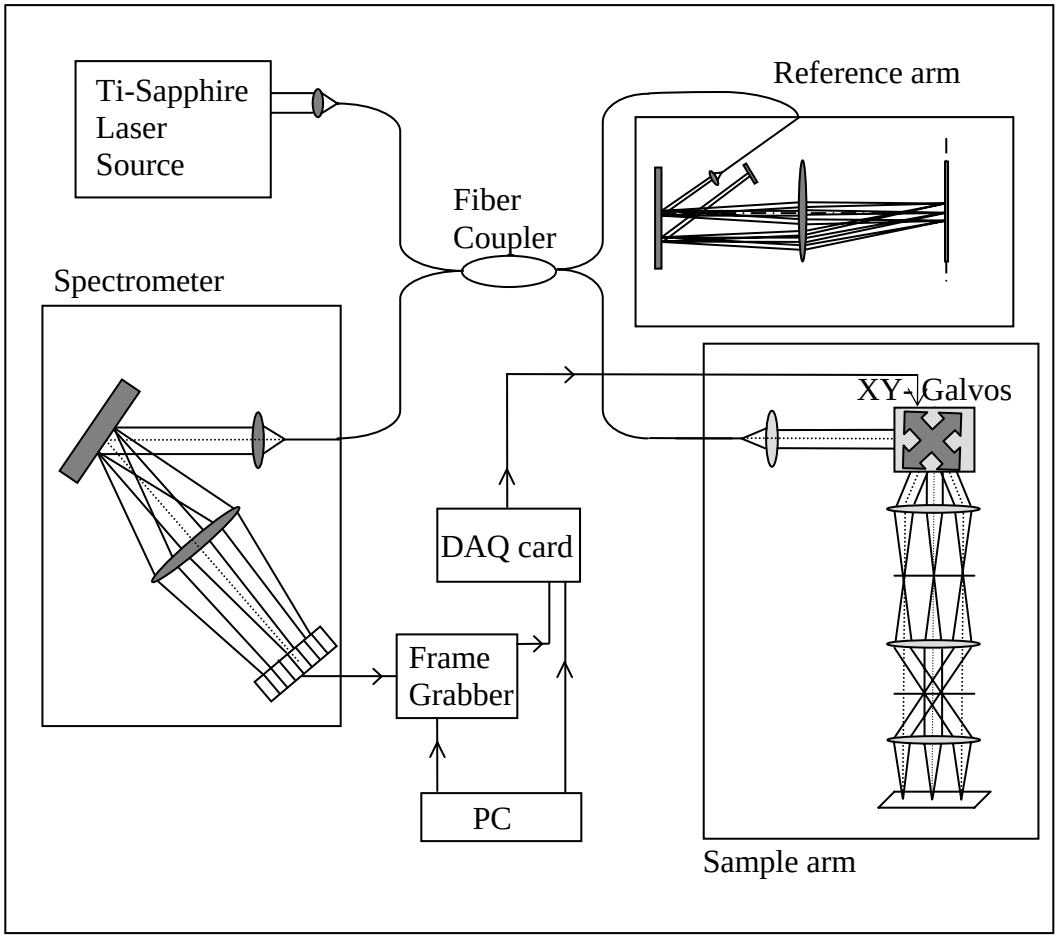


Figure 2.5: Schematic diagram illustrating the setup of FD-OCT.

A variable neutral density filter was also placed in front of the collimator to adjust the reference arm power during the experiments.

The sample path consisted of mirrors mounted on the shafts of the XY

galvanometer assembly. The light is first collimated using a collimator and then allowed to fall on the center of mirror attached to the X-galvo. This beam is then directed to the center of mirror mounted on the Y-galvo. Light from this mirror is then coupled into an objective lens through an optical relay line. The DAQ card is used to feed triangular voltage waveforms to the X-Y galvos which allowed proportionate scanning of the focused spot on the sample. The frequency and the amplitude of the scanning waveform are dictated by the required scan rate and distance. For the FD-OCT experiments conducted we were able to obtain a linear scan at frequency of 27Hz at 3volts. The construction and calibration of sample path have been detailed in [26].

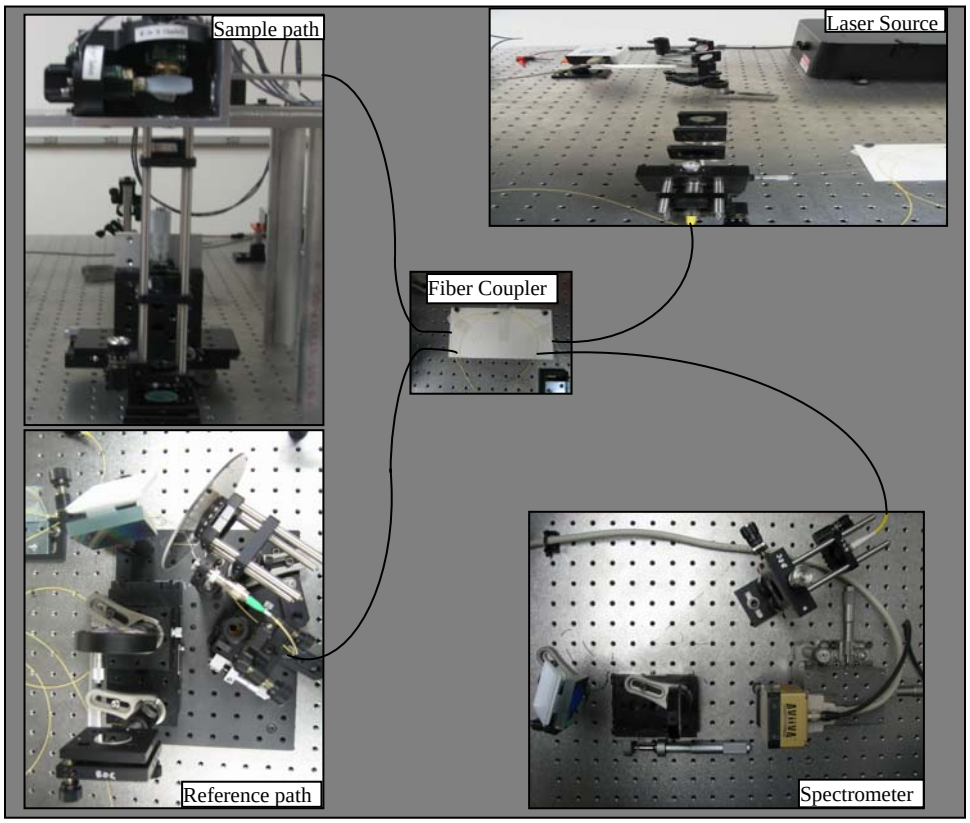


Figure 2.6: Picture of FD-OCT setup.

The spectrometer formed the detector in the FD-OCT system. Detailed description of

the spectrometer design is discussed in section 2.3. Data from the spectrometer was acquired using a frame grabber (NI-IMAQ-PCI-1428, National Instruments, Austin, TX). The data acquisition was synchronized with the scanning galvos in the sample arm using a 12 bit NI DAQ card (6052-E). Figure 2.6 shows the picture of major components of the FD-OCT setup.

## 2.3 Spectrometer Design

A ray diagram of spectrometer setup design is shown in Fig. 2.7. The spectrometer consists of a beam collimating and expanding assembly, a diffraction grating, a focusing lens and a line detector. After collimation the beam is incident on a diffraction grating where the spectrum is separated into its component wavelengths. The diffracted beam is then focused onto the array of detectors.

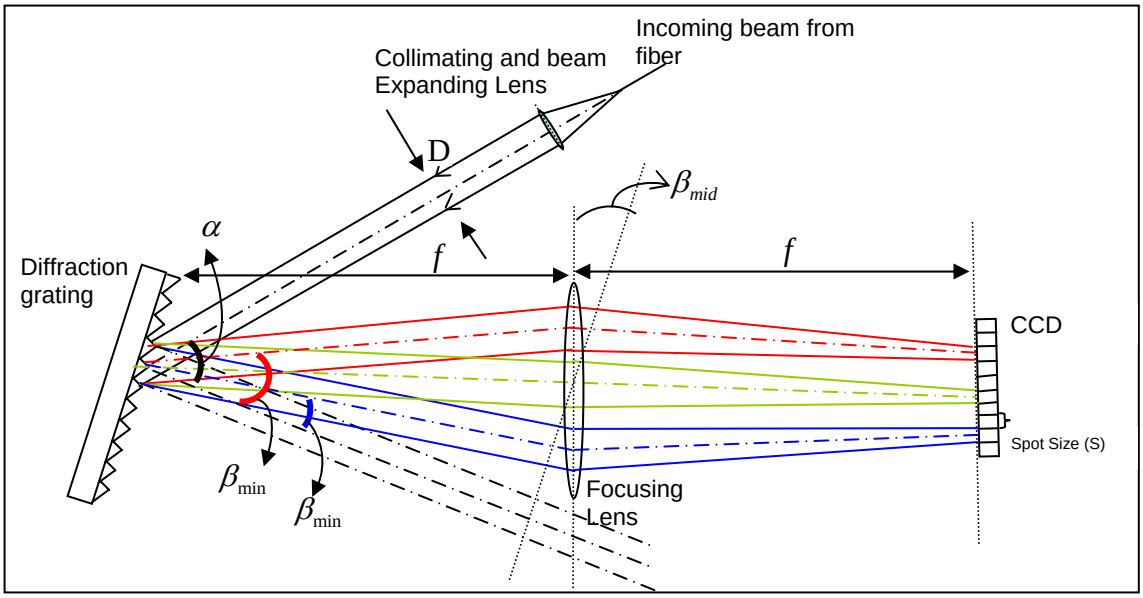


Figure 2.7: Ray diagram illustrating the working of spectrometer.

Light from the incoming fiber is first expanded and collimated using an achromatic doublet lens with 60 mm effective focal length and 55.8 mm back focal

length. The beam diameter *D* is calculated using gaussian beam optics as [25]

$$D = W(z) = w_0\left[1 + \frac{\lambda z}{\pi w_0}\right] \tag{2.26}$$

where , $W(z)$ is the beam waist at the lens and $w_0$ is mode field diameter of the fiber, and $z$ is taken as the focal length of the lens.

The expanded beam is then allowed to fall on a diffraction grating. Different wavelength components get diffracted at different angles given by the grating equation [27]

$$m\lambda = d(\sin\alpha + \sin\beta) \tag{2.27}$$

where, m represents the order of diffraction which is chosen as 1, d is the grooves spacing of the grating, $\alpha$ is the incident angle and $\beta$ is the diffracted angle. In figure 2.7, $\beta_{\max}$, $\beta_{\min}$ and $\beta_{mid}$ denote the diffraction angle for maximum, minimum and center wavelength component of the spectrum for which the spectrometer was designed. In figure 2.8 the variables and the sign convention followed for a diffraction grating is illustrated. The grating normal is the line drawn perpendicular to grating surface (figure 2.8). Differentiating equation 2.27 with respect to $\lambda$, we get angular dispersion as

$$D_A = \frac{d\beta}{d\lambda} = \frac{1}{d} m\sec\beta = Gm\sec\beta \tag{2.28}$$

where G = $1/d$ .

Thus, angular dispersion depends groove spacing in the grating. Likewise, linear dispersion (L) of a grating system is a product of angular dispersion D and the focal length ( $f$ ) and is given by

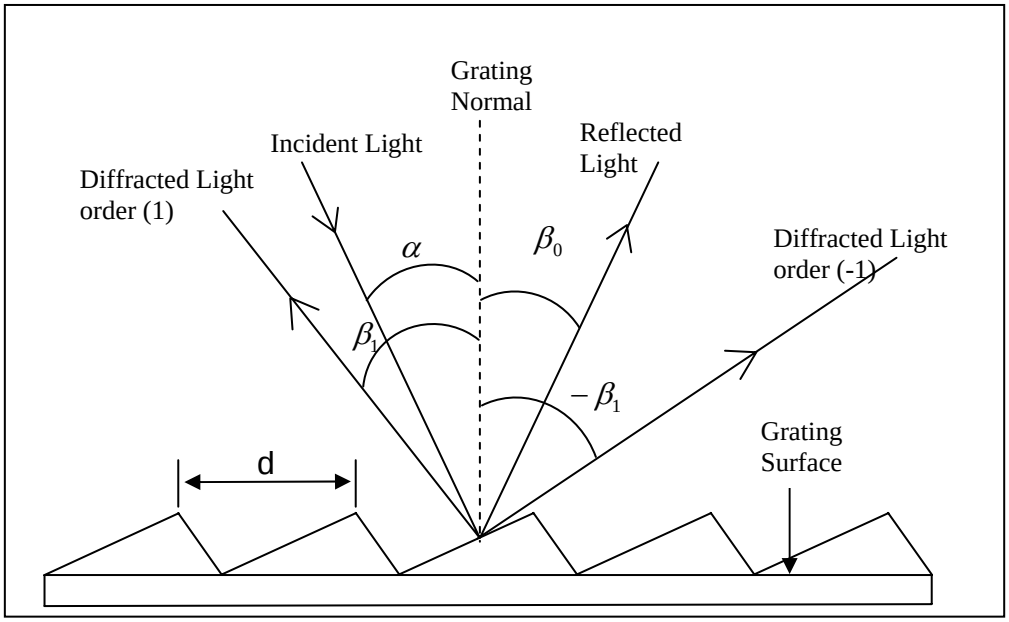


Figure 2.8: Schematic diagram illustrating grating convention and order of diffracted light.

$$L = Gm\sec(\beta) \times f \tag{2.29}$$

An important parameter that decides the resolution of spectrometer is the Plate factor, P, which is the inverse of linear dispersion and gives the change in wavelength for a given displacement along the spectrum.

$$P = \frac{d\cos(\beta)}{mf} \tag{2.30}$$

The spectrometer was deigned for a resolution of 0.1 nm.

A reflective grating with 1200 grooves/mm and an achromatic doublet of 100 mm focal length was chosen to focus the diffracted beam on the camera. The line array CCD has 2048 pixels with each pixel having size of 14 x 14 $\mu m$. All the optics was chosen for near IR (700 – 900 nm) working wavelength. Figure 2.9 (a) shows the plot of simulated results for spot size, formed at the detector versus varying wavelength.

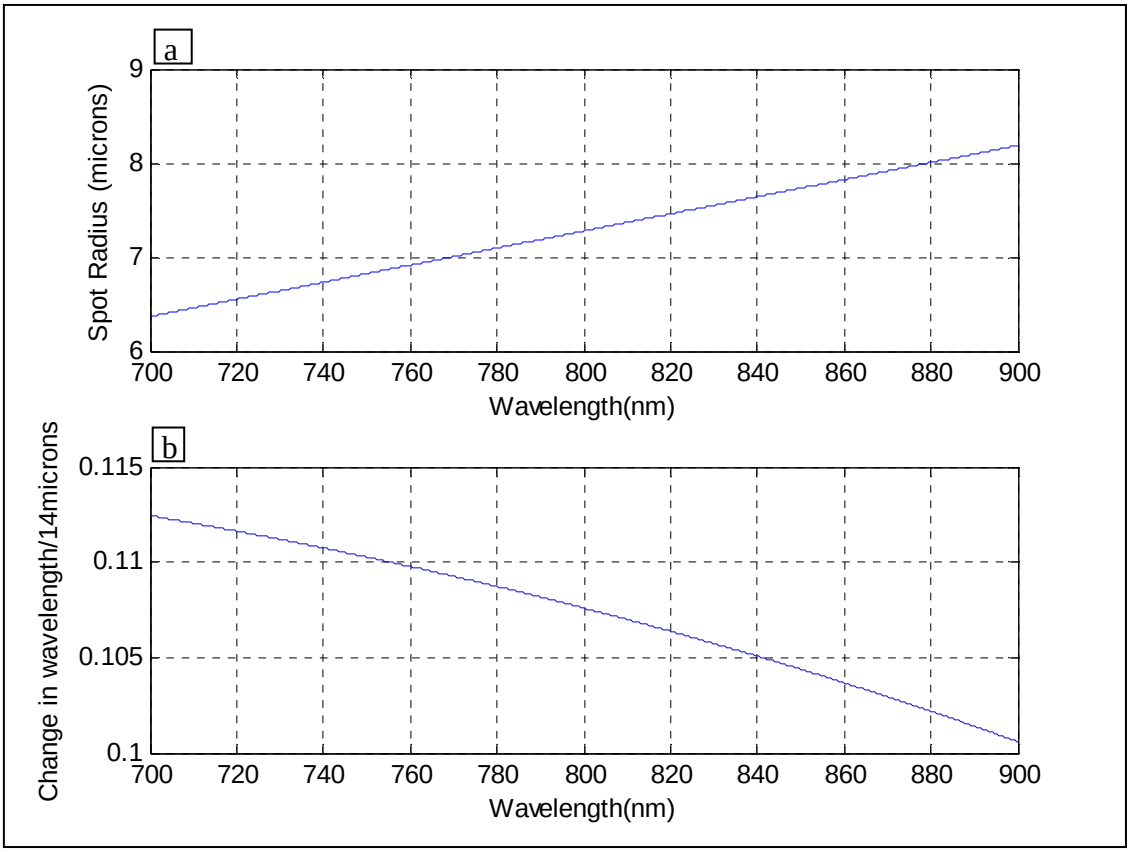


Figure 2.9: (a) Plot of spot size versus wavelength. (b) Plot of plate factor (change in wavelength per 14 $\mu$m) versus wavelength.

The spot size is calculated using equation 2.25. Figure 2.9 (b) is the plot of plate factor P, illustrating change in wavelength (nm) per 14 micron (size of detector pixel), as a function of wavelength (700-900 nm). Figure 2.10 shows the spectrometer set up and track of the light path.

The CCD linescan camera is mounted on a tip and tilt mount which is mounted on a XYZ translation stage. It was found that the focused beam incident on the CCD array was tilted in the plane of CCD array and in the plane normal to it. Tip and tilt mount holding the CCD array is adjusted to properly orient the incident focused beam. The XYZ translation stage is aligned in such a manner so that the CCD array is exactly

one focal length away from the focusing lens and fully illuminates the array pixels.

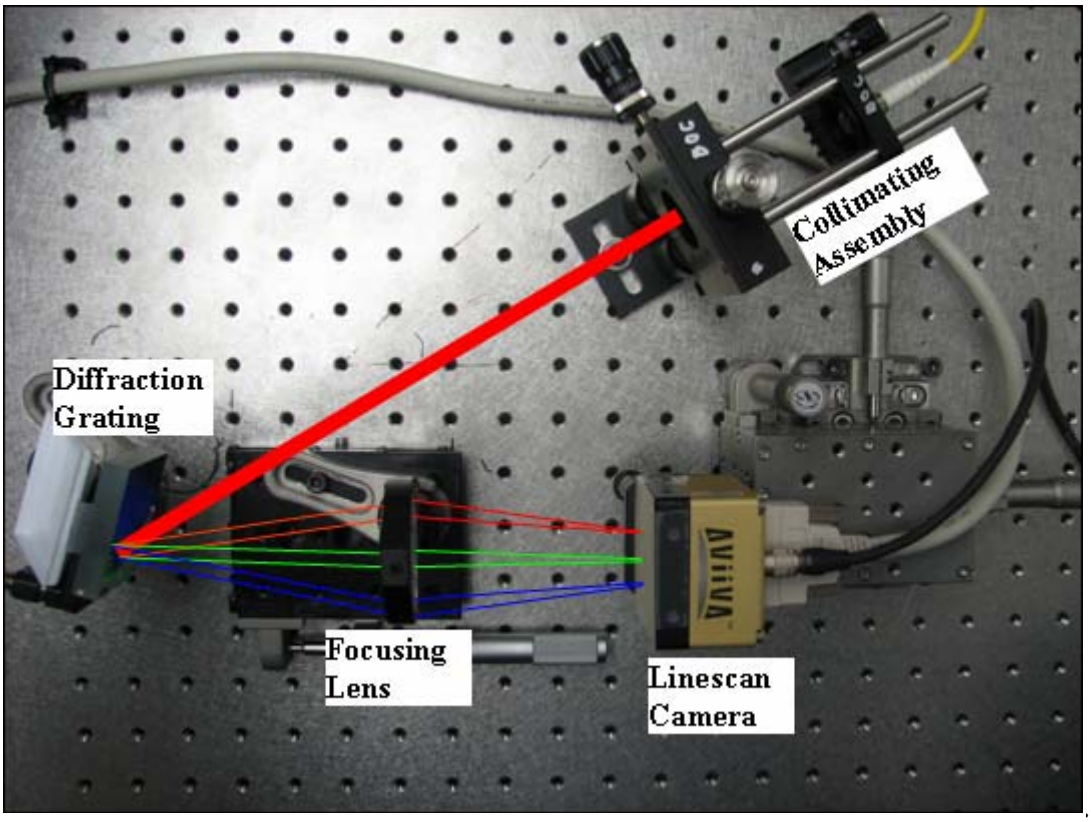


Figure 2.10: Picture of spectrometer setup.

## 2.4 Spectrometer Calibration

### *2.4.1 Wavelength Calibration*

To calibrate the spectrometer, the relationship between pixel number and corresponding wavelength needs to be established. After proper alignment of the spectrometer, this relationship was approximated as a 2nd order polynomial equation

$$\lambda_p = O + m_1 * N_p + m_2 * N_p^2 \tag{2.31}$$

where O is the constant offset, $m_1$ and $m_2$ are constant multipliers, $N_p$ is the illuminated pixel number and $\lambda_p$ is the corresponding wavelength.

To find out the values of constants O, $m_1$ and $m_2$, we recorded six sets of varying spectrum from Ti-Sapphire laser source with a commercial spectrometer (ANDO-AQ634) spectrometer and our CCD array spectrometer. Recorded spectrums were normalized. The wavelength reading from the Ando spectrometer and

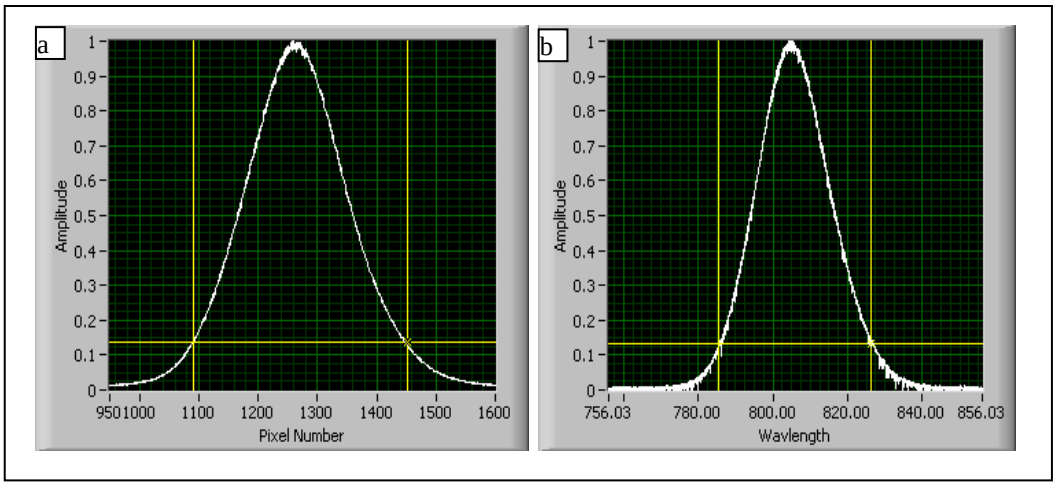


Figure 2.11: Spectrums acquired from (a) CCD Spectrometer (b) Ando Spectrometer used for calibration.

corresponding illuminated pixel number in CCD array spectrometer for each set of spectrum at $1/e^2$ ($\approx 0.135$) value, as shown in figure 2.11, were then tabulated. Thus a total of twelve set of readings, with two readings from each of the six spectrums were recorded and is tabulated in Appendix A.

Regression analysis with pixel number and corresponding wavelength gave the following parameters: Intercept O = 647.210 ; Multiplier $m_1$ = 0.1372; and Multiplier $m_2$ = -9.1604E-06. The regression statistics are shown in Table 1.

The R-square value in regression statistics suggested a good agreement for estimated intercept and multipliers. Thus, the relationship between illuminated pixel number, $N_p$

Table 2.1: Regression Statistics for calibration of spectrometer.

| **Regression Statistics** | |
|---|---|
| Multiple R | 0.9997 |
| R Square | 0.9995 |
| Adjusted R Square | 0.9994 |
| Standard Error | 0.6543 |
| Observations | 12 |

and corresponding wavelength $\lambda_p$ with current alignment of the spectrometer can be given as

$$\lambda_p = 647.219 + 0.1372 * N_p - (9.1604E-6) * N_p^2 \qquad (2.32)$$

It can be seen that the value of the multiplier $m_2$ is quite small and doesn't have a significant effect at lower values of pixel number $N_p$ corresponding to smaller wavelength. However, for larger values of pixel number, multiplier $m_2$ would have significant effect in determining the wavelength. Figure 2.12 shows the calibration results with broadband and narrow band spectrums.

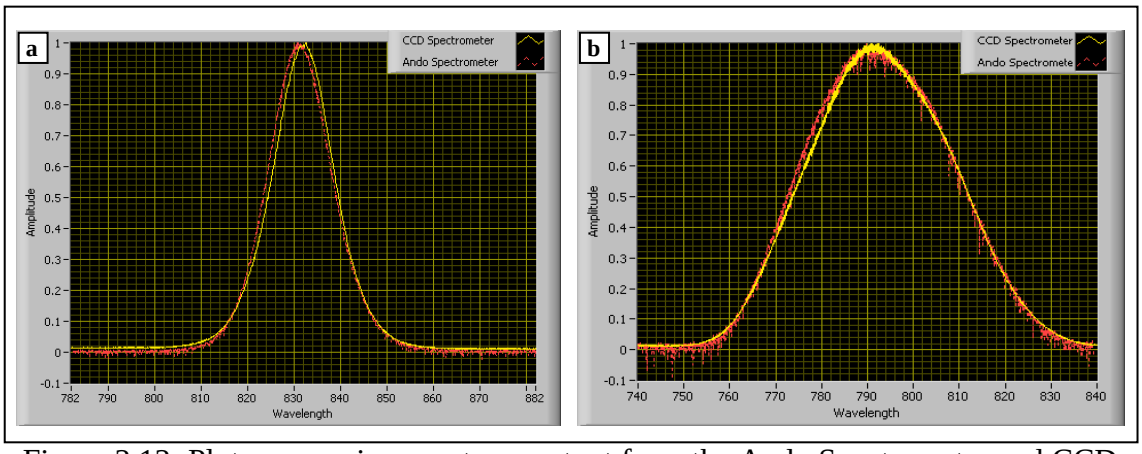


Figure 2.12: Plots comparing spectrum output from the Ando Spectrometer and CCD Spectrometer after calibration (a) Narrow band spectrum (b) Broadband spectrum.

Each plot has spectrum output from the Ando Spectrometer and CCD Spectrometer after calibration. A shift in the center wavelength and difference in full width at half maximum (FWHM) values were found between the spectrums obtained from the two spectrometers. To evaluate the error, the center wavelength and FWHM from the spectrums were obtained, after using a moving average filter to remove high frequency noise components from the spectrums. The results are tabulated in table 2.

Table 2.2: Calibration results for narrow band and broadband spectrums.

| | Ando Spectrometer | | CCD array Spectrometer | | Difference in Center Wavelength (nm) | Difference in FWHM (nm) |
|---|---|---|---|---|---|---|
| | Center Wavelength (nm) | FWHM (nm) | Center Wavelength (nm) | FWHM (nm) | | |
| Narrow band Spectrum | 831.1 | 15.7 | 832.6 | 15.4 | 1.5 (error = 0.18%) | 0.3 (error = 1.91%) |
| Broadband spectrum | 789.8 | 39.5 | 790.8 | 38.6 | 1.0 (error = 0.12%) | 0.9 (error = 2.53%) |

*2.4.2 Spectral Response of the Spectrometer*

The spectral response of the spectrometer as a function of wavelength is dependent upon the response of the diffraction grating and the array detector. The spectral response of the CCD array and grating for the wavelength range of 650-900 nm are shown in the figures 2.13 (a) and (b) respectively. The graphs were interpolated to reduce the sampling interval between wavelengths and multiplied to get overall response curve of the spectrometer. Both the factory specified response and interpolated data are shown in the graphs of figure 2.13. Figure 2.14 shows the resultant response curve of the spectrometer. The measured spectrum from the CCD array spectrometer

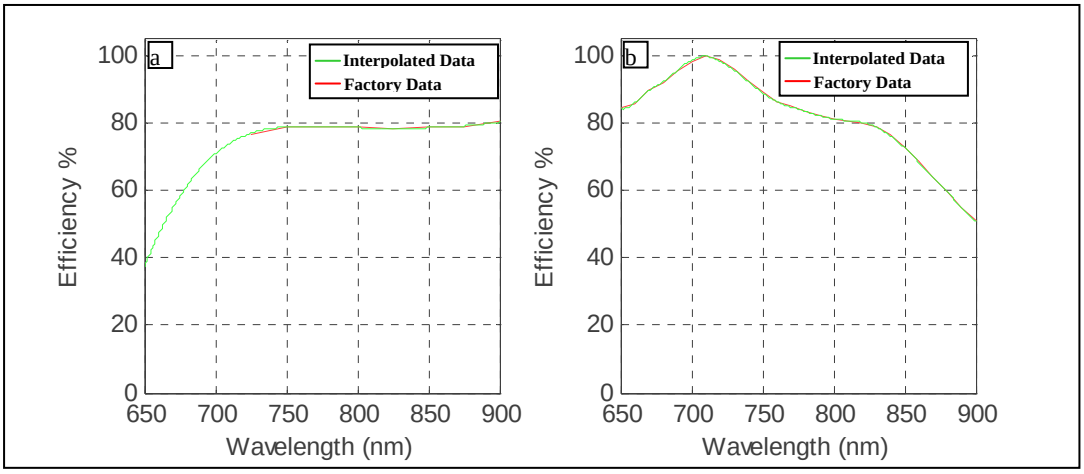


Figure 2.13: Plot of efficiency as function of wavelength for (a) Diffraction grating, (b) CCD detector.

is weighted with the spectral response of the spectrometer plotted in figure 2.14. Between 750-850 nm, the operating range of FD-OCT system, the spectral response of the spectrometer varied by 10 percent.

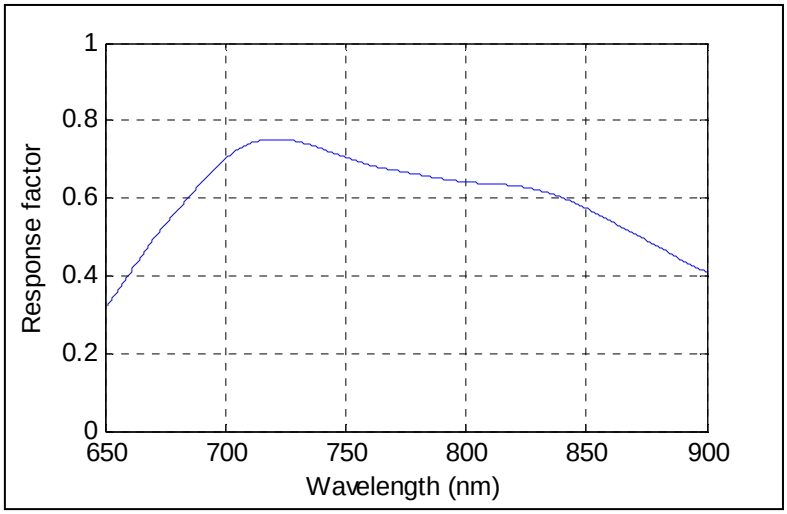


Figure 2.14: Spectral response of the spectrometer.

*2.4.3 Resolution of the Spectrometer*

The theoretical resolution of the spectrometer was calculated from plot of plate factor versus the wavelength in figure 2.9-(b). The plate factor was defined as the

change in wavelength (nm) per 14 micron (pixel size of the array).The theoretical resolution for the spectrometer was calculated as the average value of the plate factor. It was calculated to be 0.11 nm.

*2.4.4 Saturation Power of Detector Element*

The optical power P required to generate $n_e$ number of photoelectrons in the detector can be expressed as [16]

$$P = \frac{n_e h \upsilon_0}{\eta \tau} \tag{2.33}$$

where $\eta$ is the quantum efficiency of the detector, $h$ is the Planck's constant $\upsilon_0 = {}^{c}\!/\!_{\lambda_0}$ is the center frequency of the light source spectrum. The full well capacity of the CCD used is 180000 e. With our system parameters the power required to saturate each pixel of our detector is 1.684 nano-Watts.

# CHAPTER 3

# FD-OCT IMAGING

The structure and function of the FD-OCT system setup was discussed in the Chapter 2. In this chapter hardware and software interfacing of the system is presented. The software interface for the FD-OCT setup that was developed using National Instruments LabVIEW™ is also described. The data from the spectrometer is acquired using a frame grabber and a DAQ card is used to run and synchronize the galvo.

## 3.1 Spectrum Acquisition from Line Scan Camera

The CCD line scan camera is the key component of the spectrometer. The specifications of the camera are in (Appendix B). There are 2048 pixels in the CCD camera array and each pixel is a 14 micron square with a 12 bit resolution. The CCD camera supports a CameraLink data format (base configuration) with two-taps having two analog chains that process odd and even pixel outputs. The pixel array can be read out at rate of 40MHz or 60 MHz when run on the internal clock of the camera (free run mode). In the free run mode, the maximum number of line scans that can be acquire is calculated using the formulae below:

Line period = data rate period x (No. of pixels + No. of periods for charge transfer) (3.1)

Line Frequency $L_f$ = 1/Line period. (3.2)

We were able to achieve a rate of 18587 & 27881 line scans per second at 40 and 60 MHz clock frequency respectively. Read out time or the line period is thus 53.79 and

35.87 micro-seconds respectively. Figure 3.1 shows the timing diagram for free run mode.

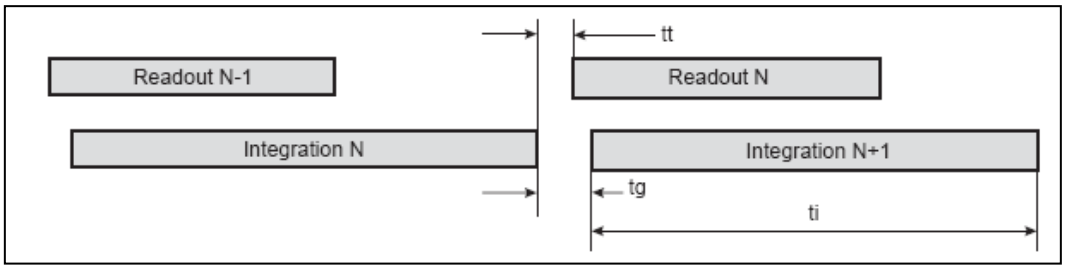


Figure 3.1: Timing diagram for camera operation.

In figure 3.1 *ti*, *tt* and *tg* denotes the integration time, delay between integration and read out, and gap between two successive integration periods respectively. Typical values of *tt* and *tg* as specified by the manufacturer are 1 micro-second and 6 micro-seconds, respectively. The integration time is specified by the user. The variation in no. of line scans per second as a function of integration was recorded experimentally and plotted in Appendix C.

High speed data transfer from the CCD camera to the PC is done with a frame grabber card from National Instruments (IMAQ-PCI-1428). The frame grabber supports Camera Link Base and Medium configurations. The PCI bus interfacing between frame grabber and the PC supports a theoretical maximum of 133 MBps data transfer rate. A MDR 26 pin connector at the frame grabber was used to connect the Camera Link Cable from the camera. A VHDCI connector in the frame grabber was used to extract Vertical Sync signal from the frame grabber. The Vertical Sync signal indicated the start of camera acquisition which was used to trigger the galvos. NI-IMAQ software was used under LabVIEW™ environment for data acquisition and subsequent

processing. A low level ring acquisition technique was employed to continuously acquire and store the data. The data acquired was stored in a binary format. Only 1024 of the center pixels were acquired at 60 MHz clock frequency so as to reduce the data stream rate from 114 MBps to 57 MBps.

The command signal to the galvos was fed using a 16 bit DAQ card from National Instruments (NI-6052 E). The galvos were run using a triangular waveform. The amplitude of the triangular waveform depended upon the area of scan in the sample path. The V-sync signal from the frame grabber was also fed to this DAQ card to initialize the scanning of galvos. The time delay between the trigger signal and settling time for the galvos was recorded and is incorporated in the processing module to eliminate the data within the settling time of galvos.

## 3.2 Lab-VIEW Interface

Lab-View virtual instrument is used as the software interface for the FD-OCT system. Five basic modules were developed to perform different operations for the user. The first module was developed for viewing the spectrum fed to the spectrometer assembly. This module is also used to determine the pathlength mismatch ($\Delta z$) between the reference arm and sample arm when the spectrometer was connected to the interferometer set up. The user also has the flexibility to operate the galvo during this operation and view the change in the modulation frequency in the spectrum. Figure 3.2 is the screenshot of the front panel of this VI. The user inputs the parameters for running the galvos. The VI shows the waveform fed to the galvos, the spectrum as from the spectrometer and the pathlength mismatch ($\Delta z$) between the reference arm and

sample arm.

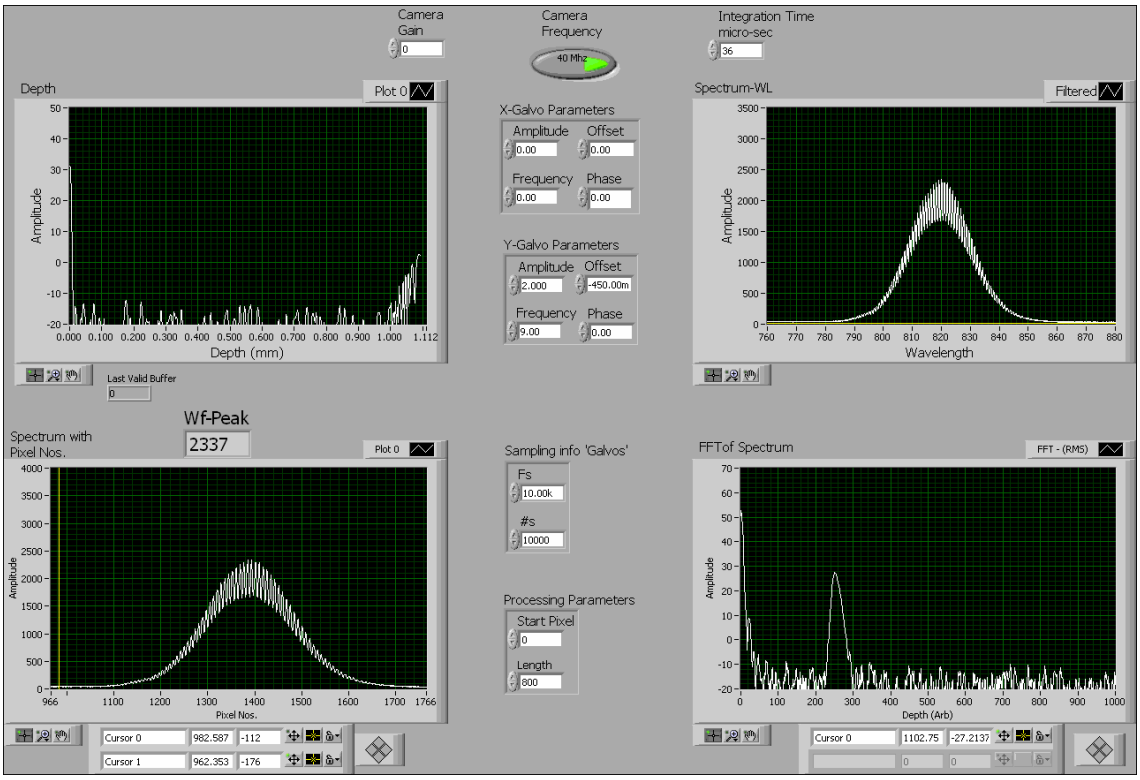


Figure 3.2: Front panel of waveform viewer VI

The second LabVIEW™ VI is used to acquire the X-Z or Y-Z scan of the sample. The user specifies the type of scan required. The user also inputs the frequency at which he wants to scan the required area. The frequency is directly coupled to the number of line scans $l_n$ to be acquired to construct a single image according to the following relation

$$l_n = \left( \frac{1}{2 \times f_{x,y}} + t_d \right) \times L_f \tag{3.3}$$

Here, $f_{x,y}$ is the frequency of x or y galvo depending upon the scan user requires. $t_d$ is the time delay between the trigger signal received and actual start of scan from one end,

which varied with scan frequency of the galvo. Time delay $t_d$ were determined for all the operational frequencies of the galvo and incorporated into the module for acquisition of image. 1000 linescans are acquired per frame and number of frames to acquire is computed by the VI by rounding off number of linescans per 1000, $\left( l_n / 1000 \right)$, to next integer value. Figure 3.3 is the timing diagram for X-Z or Y-Z scan. It illustrates the timing of V-sync signal from the frame grabber that is used to trigger the galvo and the position signal obtained from the galvo. Only the data within time $t_{dr}$,

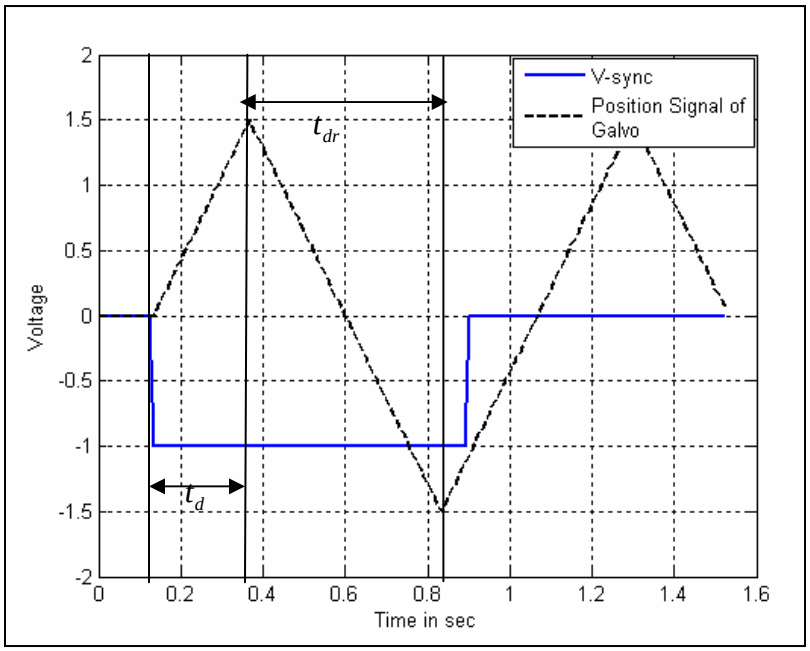


Figure 3.3: Timing diagram for X-Z or Y-Z B-scan.

after time $t_d$, is used to construct one B-scan. $t_{dr}$ is calculated as

$$t_{dr} = \frac{1}{2 \times f_{x,y}} \tag{3.4}$$

Thus from the total number of linescans obtained, initial $t_d \times L_f$ lines were ignored and thereafter $t_{dr} \times L_f$ lines were used to construct one image. Figure 3.4 shows the flowchart for this VI. At the beginning, a header file is created with name, timestamp with date, sample description, scanning parameters and camera settings. Next the camera is initialized whereby a command signal is sent to the camera containing information of integration time, output frequency, acquisition width, odd and even pixels gain and offset. Once the initialization is done, a buffer is created in the RAM to store all the acquired linescans. Data acquired is then converted to binary format, and is stored in the hard disk with the header file created initially. The data is also passed on to a Sub-VI for image processing. The processed data is finally stacked using the scan parameters and displayed to the user. Fig 3.5 shows the front panel of the VI.

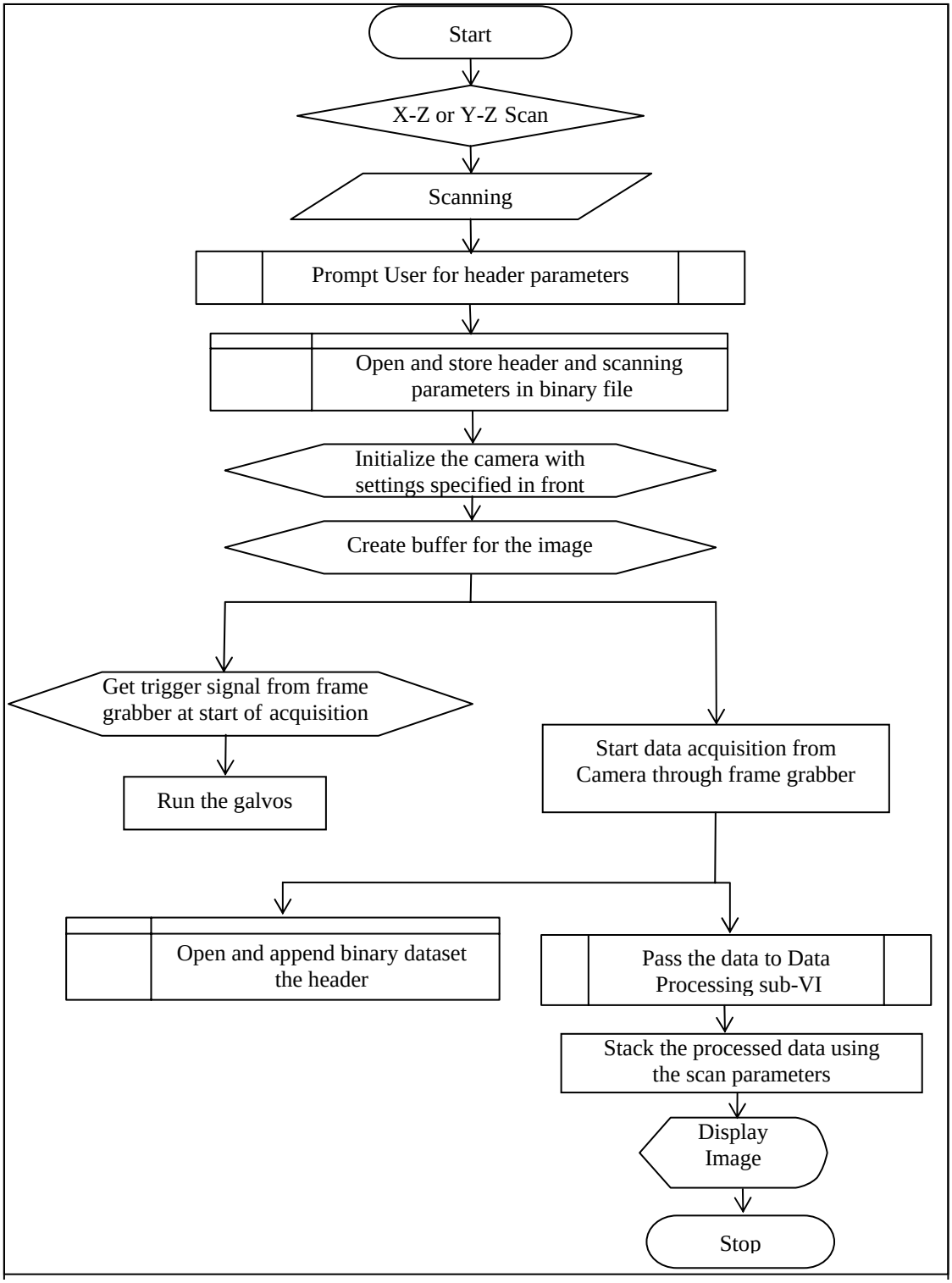


Figure 3.4: Flow chart of VI for X-Z or Y-Z B-scan.

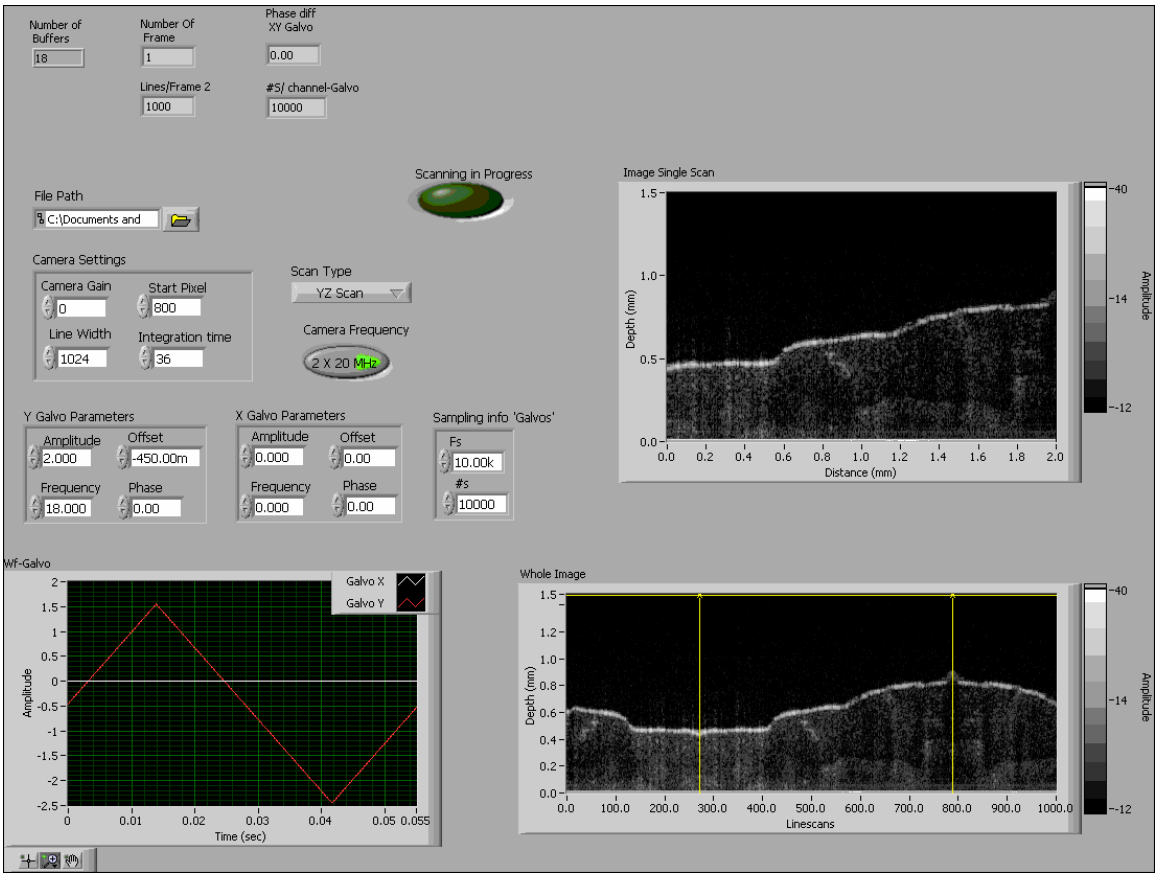


Figure 3.5: Front panel of VI for image acquisition with X-Z or Y-Z B-Scan.

The third VI is the data processing VI. It takes 2-D data containing stacked linescans of spectrums acquired. It then converts the spectrums from $\lambda$ to K-space. The conversion to $k$-space involves the resampling of data into equal intervals. Cubic-spline interpolation is used for evenly resampling the data evenly in $k$-Space. Thereafter, FFT of the data is taken and scaled to logarithmic value. The time taken to process a single image containing 1000x800 pixels with interpolation and FFT is approximately 4 seconds. Figure 3.7 is the schematic for operations involved in this sub-VI.

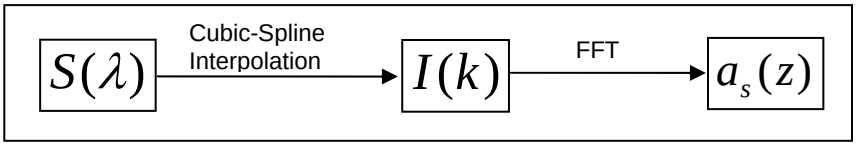


Figure 3.6: Block Diagram for Data Processing.

The fourth VI was written to acquire enface image of a sample. Most of the features of this VI was similar to that of XZ or YZ scanning VI, however both the X and Y galvos are operated to acquire the enface image. To acquire the enface image, the sample is raster scanned in the XY plane and depth profile at each point is obtained through the spectrum. Thus, a 3-D volumetric data is acquired. The timing diagram with position signal of X and Y galvo and the V-sync signal from the frame grabber are shown in figure 3.7.The slow galvo is given a ninety degree phase shift so that it starts from end of the image to be scanned. Initial $t_d \times L_f$ lines are discarded. Each B-scan is constructed by taking $t_{dr1} \times L_f$ number of lines, where $t_{dr1}$ is given as

$$t_{dr1} = \frac{1}{2 \times f_{fast}} \tag{3.5}$$

with $f_{fast}$ being the frequency of fast galvo. A total number of $t_{dr2} \times L_f$ linescans are retained to make a volumetric image where $t_{dr2}$ is given as

$$t_{dr2} = \frac{1}{2 \times f_{slow}} \tag{3.6}$$

with $f_{slow}$ being the frequency of slow galvo.

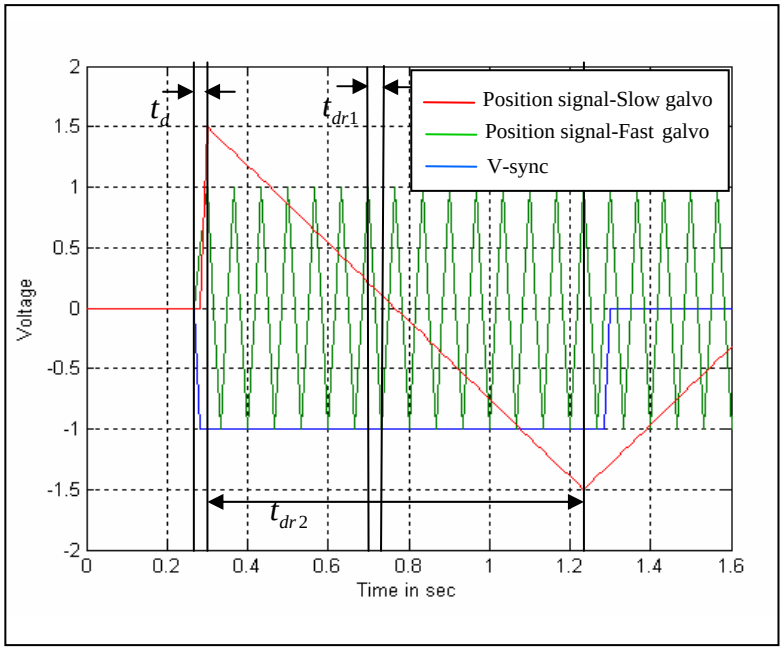


Figure 3.7: Timing Diagram for 3D Scan.

Later this data is processed by another VI. The user decides the depth at which he is interested to reveal the surface tomography. A slice of this 3-d volumetric scan is then extracted. For our purpose, we moved the X galvo slower and Y galvo faster. The resolution along Y and X plane is given by following.

$$R_y = l_y \Big/ \left(\frac{1}{2\times f_y} \times L_f\right) \tag{3.7}$$

$$R_x = \frac{l_x}{2} \cdot f_x / f_y \tag{3.8}$$

where $l_y$ and $l_x$ are the distance scanned in x and y direction respectively. The final VI, FD-OCT-Image-Processing VI, is written to retrieve the images from data files that have been scanned earlier. This VI first opens up the header file and reads the important processing parameters like scanning galvos frequency and amplitude, type of scan,

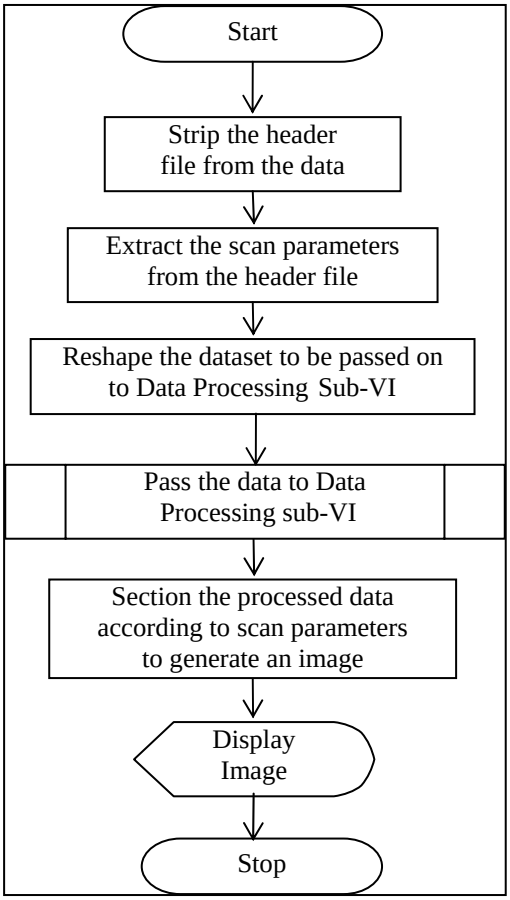


Figure 3.8: Flowchart for FD-OCT Image processing VI.

number of line scans acquired and camera settings during the scan. These parameters are used to provide the information how the scans have to be stacked for image formation. Next the Data Processing sub-VI described earlier is called and processing is done for all the line scans. The processed data is then sequentially stitched according to the scan parameters to form an image. Figure 3.8 shows the flow chart for the image processing VI.

## 3.3 FD-OCT System Characterization

In this section, performance of the FD-OCT system is discussed. System characterization with maximum measurable depth, depth resolution and lateral resolution of the system are presented. Noise sources and the signal to noise ratio of the FD-OCT system are also presented.

### *3.3.1 Maximum Depth*

Maximum measurable depth of the FD-OCT system depends upon the resolution of the spectrometer. To find out the maximum depth measurable by our system, the position of the reference mirror was varied keeping the mirror in the sample path at the focus. The maximum measurable depth was recorded as 1.54 mm.

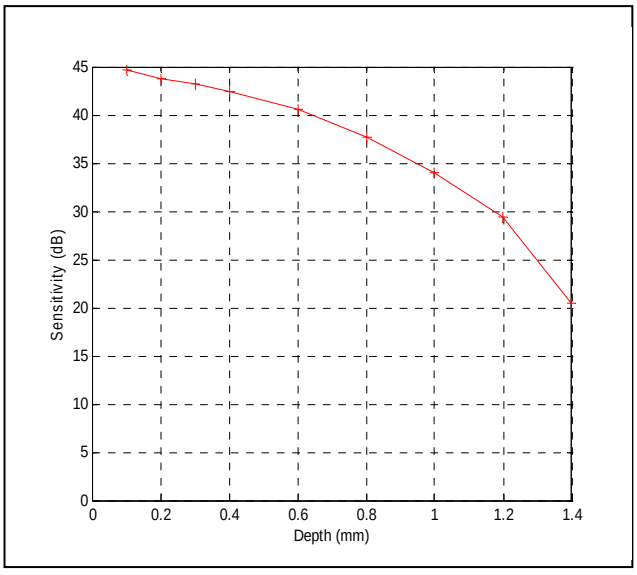


Figure 3.9: Plot of Sensitivity Vs Depth.

The sensitivity of the system was found experimentally for varying depths for a mirror surface and is plotted in figure 3.9. It was observed that the sensitivity decreased with the increase in depth. The decrease in sensitivity is attributed to the finite

resolution which decreases fringe visibility as modulation frequency increases.

*3.3.2 Depth Resolution*

The theoretical axial resolution of our system as calculated using equation 2.17 is for center wavelength of 820 nm and FWHM of 30 nm is 9.87 nm. Depth resolution of the system was experimentally found out from the FWHM of the point spread function. Figure 3.10 shows the plot of axial resolution at various depths. Deterioration in the axial resolution was found as we moved in depth, due to errors introduced in interpolation process from λ to k space at higher frequencies.

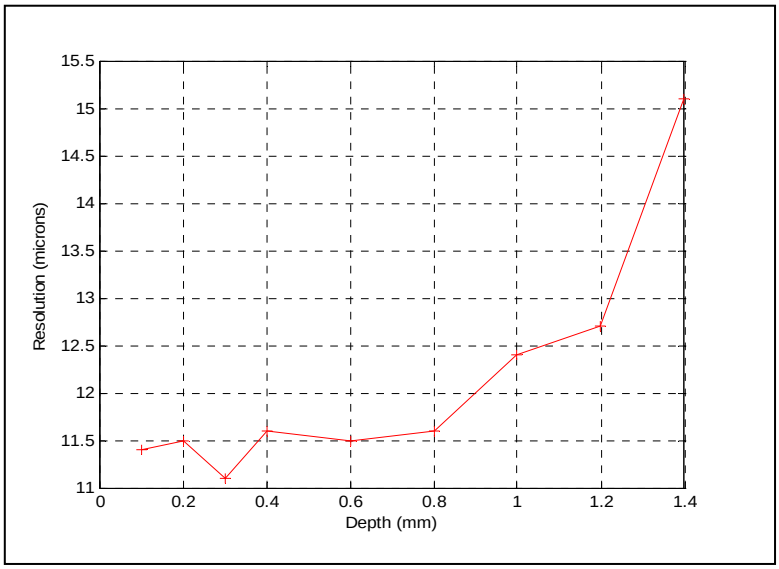


Figure 3.10: Plot of resolution as a function of depth.

*3.3.3 Signal Analysis of the FD-OCT system*

3.3.3.1 Fixed Pattern Noise

The spectrometer in the FD-OCT system could be operated at clock frequency of 40 MHz or 60 MHz. At clock frequency of 60 MHz, fixed pattern noise of 10 MHz, 20 MHz and 30 MHz originated from the camera. Similar noise appeared at 10MHz and

20 MHz when the camera was operated at clock frequency of 40 MHz. This caused a fixed pattern noise to appear in the images. Figure 3.11 shows the FFT of data acquired from the camera at dark conditions.

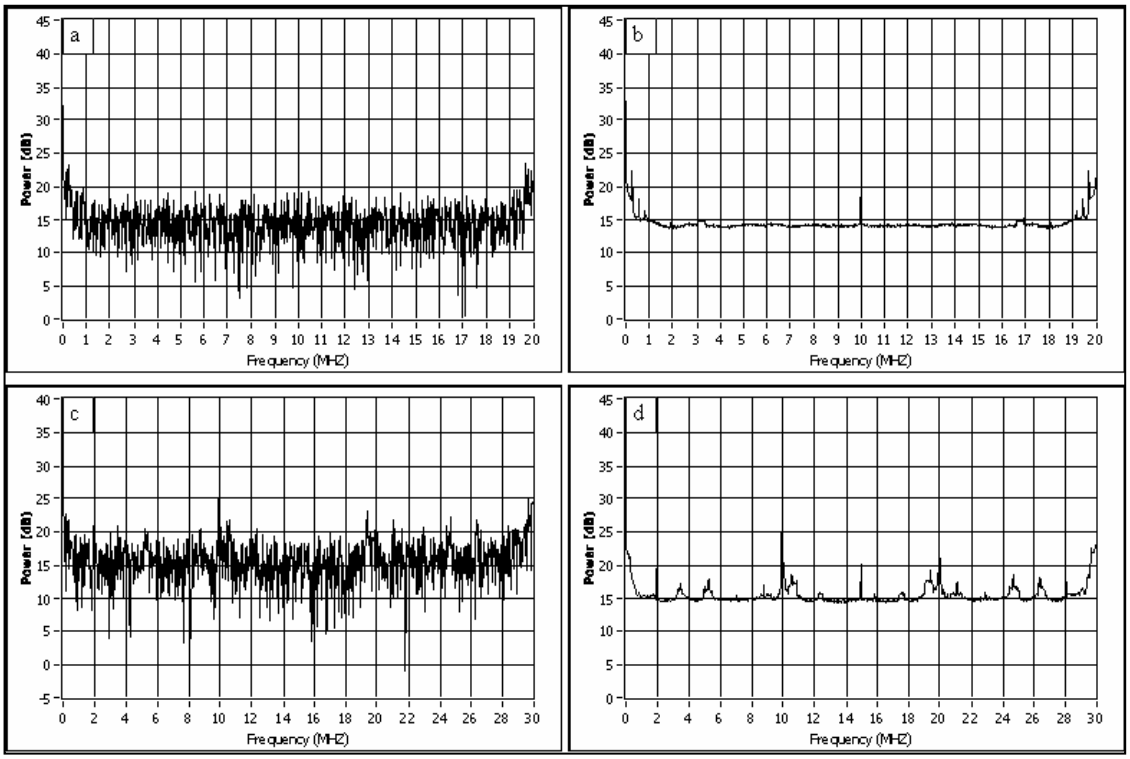


Figure 3.11: Plots of FFT of spectrum acquired at 40 MHz (a and b) and 60 MHz (c and d). Plots (a) and (c) are FFT of single spectrum. Plots (b) and (d) are averaged FFT of 1000 spectrums.

Several techniques were tested to minimize the noise in both the cases. In the first method the additional reference spectrums were acquired by closing the sample path after imaging the sample. The spectrums thus acquired were subtracted from the interference spectrum before processing the data and constructing the image.

In the second method, a reference image was constructed from the spectrums obtained from the reference path only after imaging the sample. The reference image was then

subtracted from the original image. This technique however resulted in loss of information in the noise bands.

The third technique from [33] was more computationally involved. In this technique averaged FFT of 1000 reference waveforms were taken. The averaged FFT was then subtracted from the FFT of the interference signal. The inverse Fourier transform of the resultant data was then taken after zero padding to construct the interference spectrum. Finally this data was passed through the data processing process of FD-OCT as described in the previous section. This helped to reduce the pattern noise from the system. Figure 3.12 shows the original image and the image obtained after preprocessing the data with the first and third techniques described.

Another important source of noise in the FD-OCT is the appearance of mirror images due to frequency ambiguity. As the images are obtained by taking the FT of the interference spectrum the resulting image is accompanied by a symmetric image about $z = 0$. The mirror image may overlap with the actual image structure if the object is placed improperly with respect to reference plane. Thus the mirror in the reference arm should be placed in such a way that the entire object is placed one side of the reference plane.

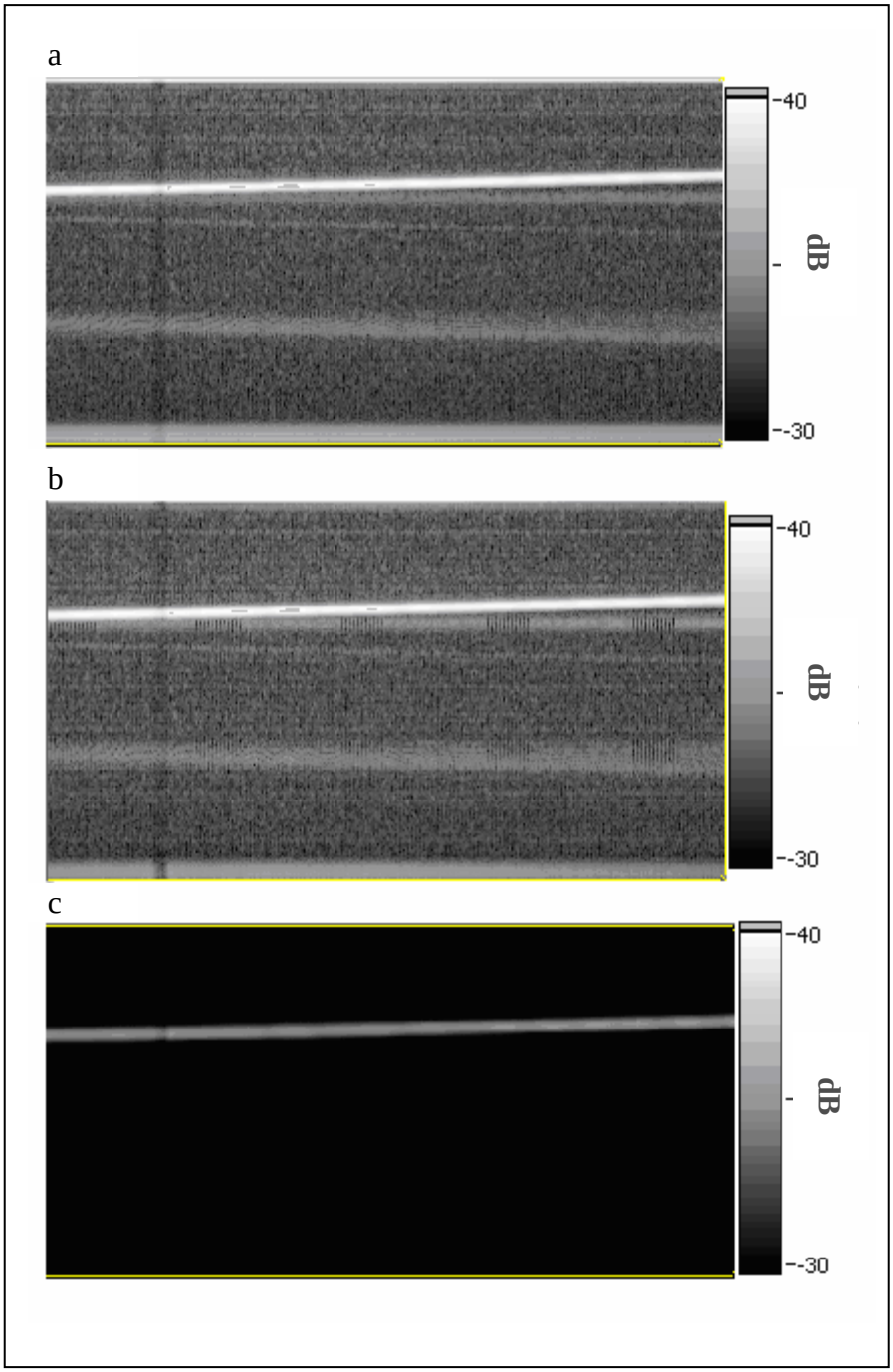


Figure 3.12: Images of mirror acquired at 27 Hz. (a) without any preprocessing (b) after subtracting the reference arm spectrum (c) image processed with the final technique.

*3.3.3.2 Signal to Noise Ratio*

Signal-to-noise (SNR) ratio characterizes the measurement performance of the system. Noise sources in an OCT system are electrical or optical in origin. These noise sources include detector noise such as thermal noise, digitization noise and readout noise, shot noise, and relative intensity noise [15]. Maximum SNR is obtained when shot noise dominates the detector noise and RIN. If sample arm power is much smaller than the reference arm power, which is true in case of tissue samples, then shot noise will dominate RIN when the following condition is met for a single detector element per readout cycle [28]

$$P_r < \frac{E_\nu}{\tau_c \eta} \tag{3.9}$$

where, $P_r$ is the reference power, $E_\nu$ is the photon energy at center frequency ν and $\tau_c$ is the coherence time given by $\tau_c = l_c / c$.

With our system parameters, for shot noise limited operation, the reference arm power at a single pixel of detector element should be less than 26 nano-watts. This will always be true since the each detector element gets saturated at 1.634 nano-watts. At shot-noise limited performance, the theoretical SNR for SD-OCT system is given by [14].

$$SNR = \frac{\eta P_s \tau_i}{h\nu} \tag{3.10}$$

where, $P_s$ is the sample arm power, $\tau_i$ is the integration time and $h$ is the Planck's constant. Thus, the SNR for an FD-OCT system is bandwidth independent.

The signal to noise analysis for the FD-OCT system was done for a perfectly reflecting surface and a weakly reflecting surface using a mirror and a glass slide respectively. The SNR of the system was defined as

$$SNR = 20\log_{10}\left(\frac{S_{\max}}{\sigma}\right) \tag{3.11}$$

$S_{\max}$ is the maximum signal intensity and $\sigma$ is the standard deviation of the noise floor. SNR was found for the varying input power to the interferometer. SNR was measured at both 0db gain and exposure time of thirty-six micro-seconds. The plots of SNR for mirror and glass-slide are shown in figure 3.11 (a) and (b) respectively. For mirror it was seen that the signal to noise ratio increased steadily with an increase in input power to the spectrometer. However increasing the input power beyond 0.12 milliwatts did not cause a significant increase in the SNR. The maximum SNR for mirror was found to be 52.05 dB. For a glass slide similar trend was observed initially, however, the SNR stopped increasing after the input power of 0.47 milliwatts to the interferometer. The maximum SNR for glass slide was found to be 55.10 dB.

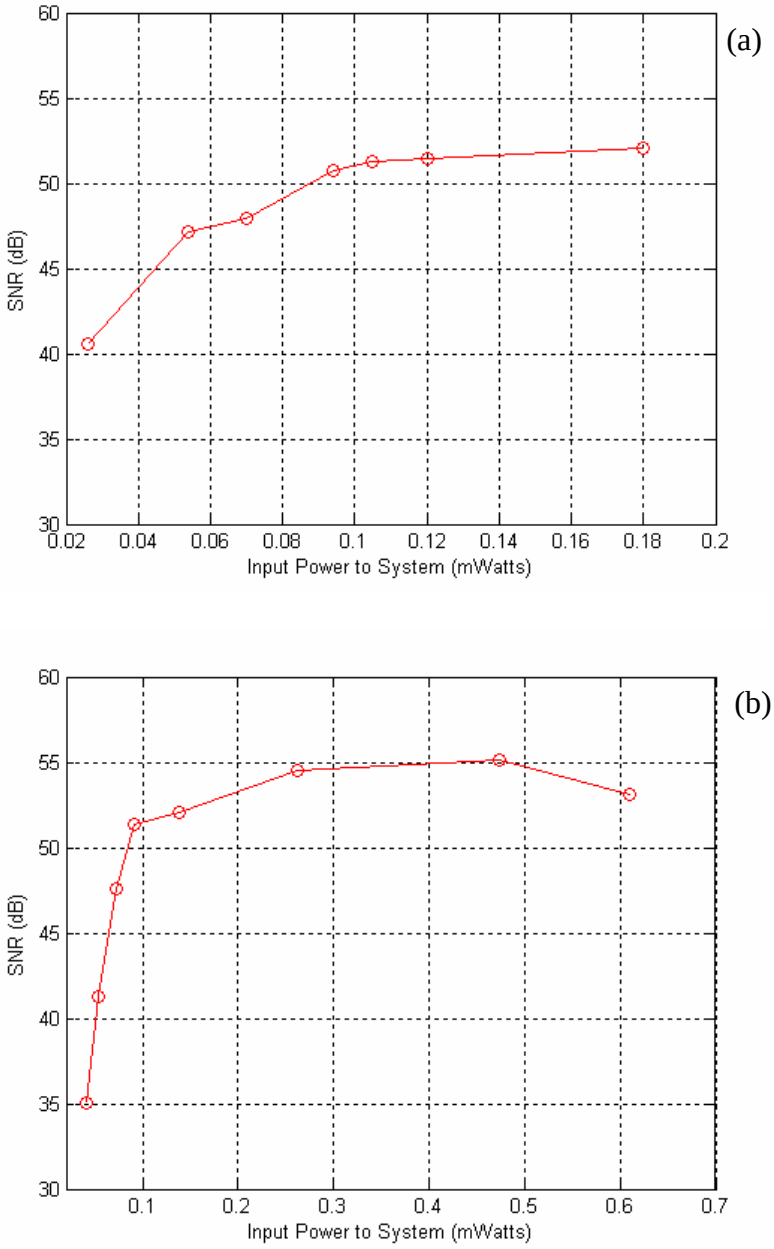


Figure 3.13: Signal to Noise ratio at 0 db (a) mirror (b) glass slide.

# CHAPTER 4

# RESULTS AND DISCUSSION

In this section we present images of some biological samples acquired with the FD-OCT system. FD-OCT images of human finger and discarded tissue samples of rabbit are presented. Finally an image of a stack of cover slip acquired at 27 Hz is shown, demonstrating the video-rate acquisition capabilities of the system.

## 4.1 Image of an Onion

Figure 4.1 shows image of an onion acquired using the FD-OCT system. Onion cells are very large, in the order of a few hundred microns. The image was acquired at a frame rate of 9 Hz and consisted of 1032 transverse and 400 axial pixels. This covered a depth of 1.4 mm and transverse length of 2 mm.

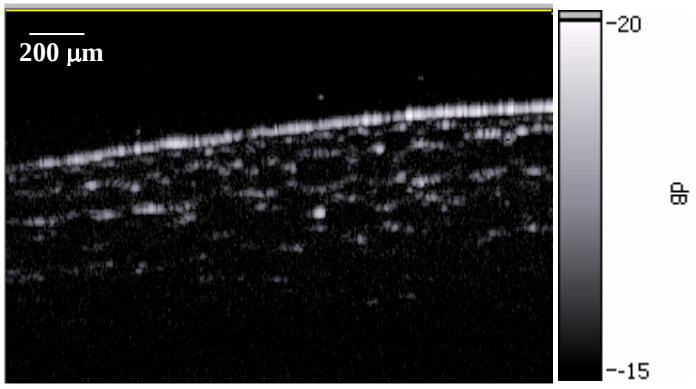


Figure 4.1: Image of an onion

## 4.2 Tissue Images

### *4.2.1. Images of Human Finger*

Figure 4.2 and 4.3 shows the images acquired from a finger of a human volunteer. Image in figure 4.2 is acquired from the nail and skin interface of the middle finger of the volunteer. The images were acquired at 18 Hz and comprised of 400 axial and 517 traverse pixels. The exposure time for the camera was set to thirty-six micro seconds. In figure 4.2 the nail and skin juncture is clearly visible. Image in figure 4.2 is acquired from dorsal portion of the finger.

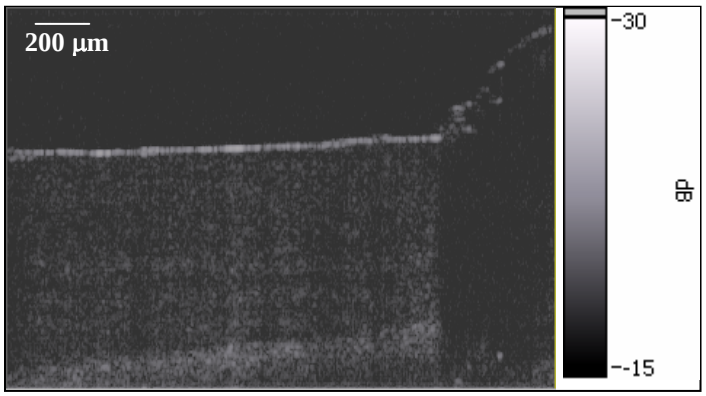


Figure 4.2: Image acquired from nail skin interface of a human finger.

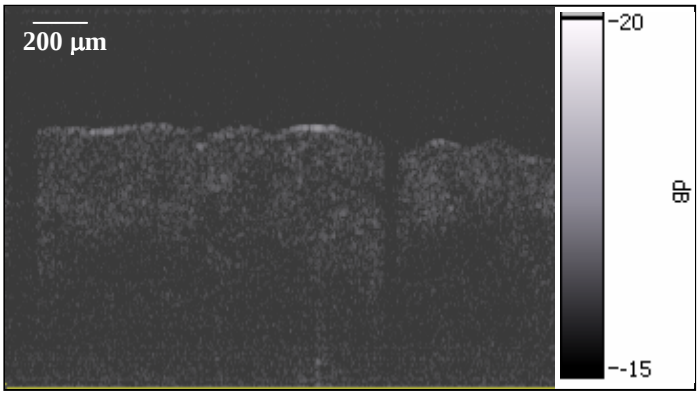


Figure 4.3: Image acquired from dorsal portion of human finger.

The position of the mirror in the reference path was carefully adjusted during imaging to avoid overlapping images. The power in the reference path was also adjusted during imaging with the help of a variable neutral density filter to get maximum SNR.

*4.2.2. Images of Rabbit Esophagus*

Ex-vivo OCT images of esophagus were acquired at 18 Hz from discarded tissue sample of a rabbit. To prevent the desiccation the tissue sample was kept in DMEM (Dulbecco's Modified Eagle's Media). The images were acquired within two hours from tissue extraction. Figure 4.4 (a) and (b) are the images obtained from different locations on the sample.

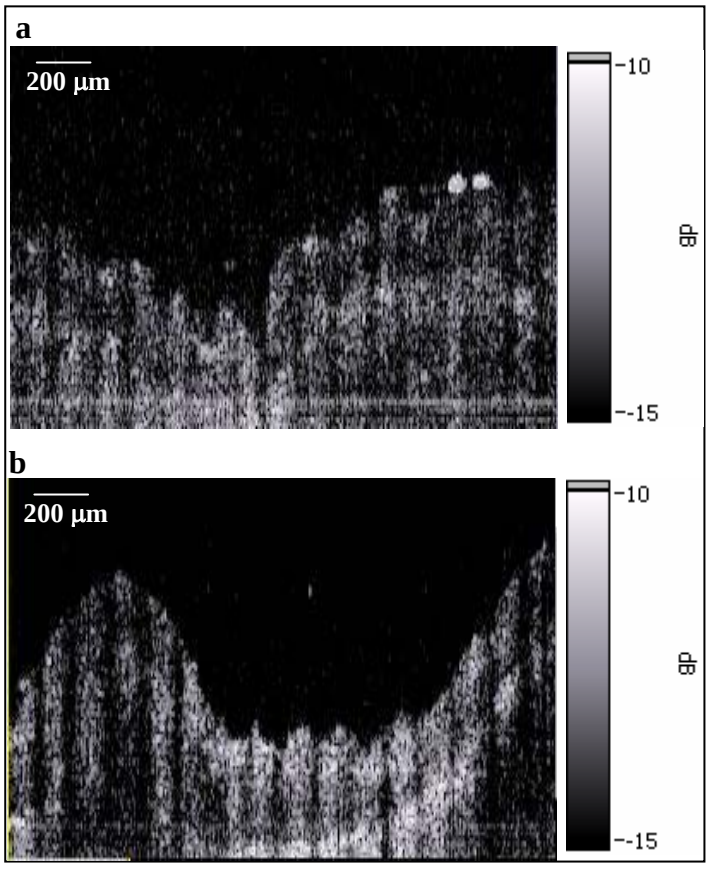


Figure 4.4: Images acquired from esophagus of a rabbit

The images consist of 517 transverse and 400 axial pixels corresponding to 2mm and 1.4 in depth respectively.

*4.2.3. Images of Rabbit Bladder*

Figure 4.5 (a) and (b) are the images of bladder acquired from different locations of discarded tissue sample of the rabbit. The tissue sample was kept in DMEM and the images were taken within two hours from tissue extraction. The images of the bladder were acquired at 18 Hz. The images consist of 517 transverse and 400 axial pixels.

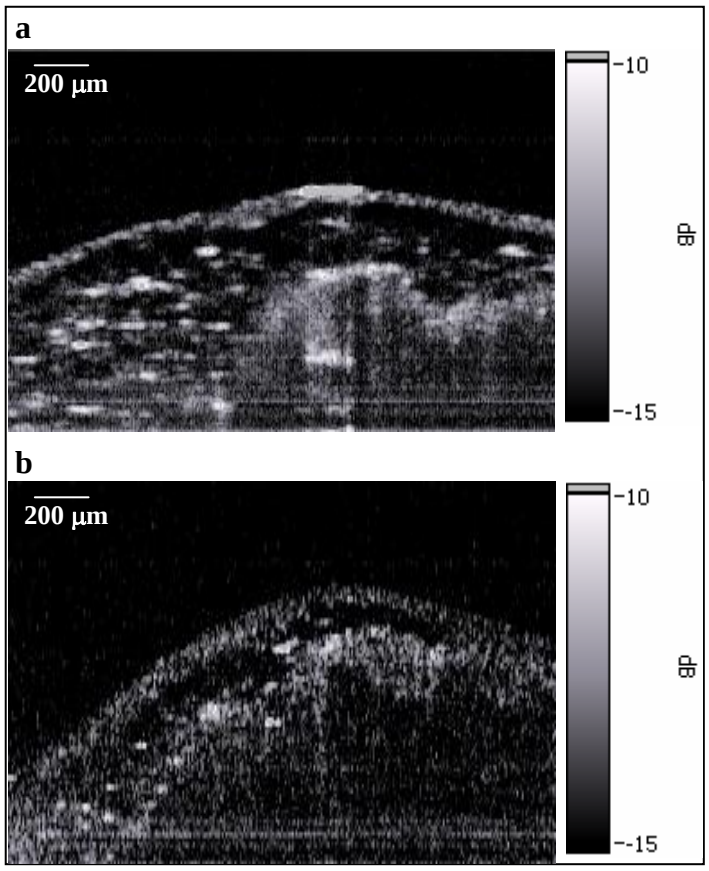


Figure 4.5: Images acquired from bladder of a rabbit

## 4.3 Video-Rate Acquisition using FD-OCT

The images discussed in the previous sections were acquired by setting the internal clock frequency of camera at 40MHz. However to demonstrate the video-rate acquisition of the FD-OCT system, the camera is operated at the internal clock speed of 60 MHz, acquiring 27880 lines per second. To bring down the data transfer rate only 1024 pixels containing the required spectral information are acquired. Running the galvos at 27 Hz then allowed us to collect 27 frames of image per second. However at internal clock speed of 60 MHz the camera generated distinct pattern noise which required additional pre-processing of the data to clean up the image.

A sample consisting of three cover slips, separated from each other by double stick tape was imaged at 27 Hz. Figure 4.8 shows the image of the fifth frame of this sample. The image was reconstructed after performing the preprocessing as explained in section 3.3.1.

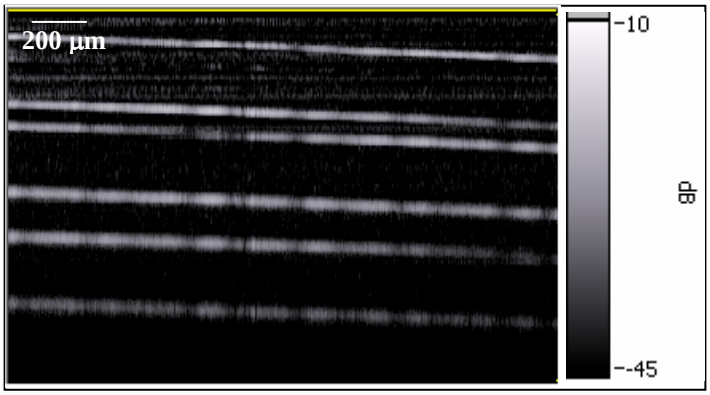


Figure 4.6: Image of stack of 3 cover slips acquired at 27 frames per second

The top and the bottom surfaces of the three cover slips are distinctly visible in the image. Multiple reflections within the sample gave rise to noise visible in the upper

portion of the image. The pre-processing technique has helped to reduce the pattern noise in the images.

# CHAPTER 5

# CONCLUSION

A fast spectrometer capable of operating 27.8 kHz has been constructed and calibrated with a resolution of 0.11 nm. FD-OCT has been implemented with this fast spectrometer. The system is capable of acquiring images at up to 27 Hz with 517 transverse pixels per frame. Imaging at the rate of 18 Hz has been demonstrated with biological samples like onion and tissue. To acquire process and display a single B-scan the system took approximately 4 seconds. The system has an axial resolution of 12 micrometer and the signal to noise ratio has been evaluated to be 59.4 dB.

The axial resolution of the system is dependent upon the resolution of the spectrometer. Less than half of the total numbers of pixels in the line detector are currently employed to view the interference spectrum. The resolution of the spectrometer could be increased by using longer focal length focusing lens and fully utilizing the line detector array. The transverse resolution of the system could also be enhanced by incorporating objective lens of higher magnification. Currently the images are acquired with a 25.4 mm objective lens with 10x magnification in the sample path.

The pattern noise that shows up at higher image acquisition rate, with the system also needs to be addressed. Though these noises were shown to be reduced by preprocessing the acquired data, it caused blurring in the resultant images. More efficient filtering algorithms could be employed to obtain higher quality images.

One of the main limitations of the current system lies in the processing speed. Though the system is capable of acquiring data at close to video-rate the image display rate of the system is slow. This limitation is due to the fact that the system currently relies on the general purpose algorithms developed by Lab-VIEW™ for FFT and interpolation during processing the data. Use of custom built algorithms developed on C or Visual C++ platforms could help to overcome this limitation. Further, use of multi threading to run acquisition and processing on separate threads using processors with hyperthreading technologies, could help the system to perform real-time image display with acquisition at video-rate.

Overall there is lot of room for improvement of the FD-OCT system developed and with enhancements listed above, it is hoped that the system could be successfully used in the near future for numerous clinical trials and applications.

# APPENDIX A

## DATA TABLE FOR CALIBRATION OF SPECROMETER

| Wavelength Ando Spectrometer | Pixel number CCD array Spectrometer |
|---|---|
| 762.619 | 894 |
| 824.594 | 1432 |
| 766.309 | 930 |
| 823.032 | 1425 |
| 785.954 | 1088 |
| 826.417 | 1450 |
| 793.301 | 1144 |
| 840.442 | 1574 |
| 804.582 | 1246 |
| 844.708 | 1605 |
| 817.139 | 1363 |
| 846.004 | 1629 |

# APPENDIX B

## PLOT OF LINE FREQUENCY VERSUS INTEGRATION TIME FOR LINE SCAN CAMERA

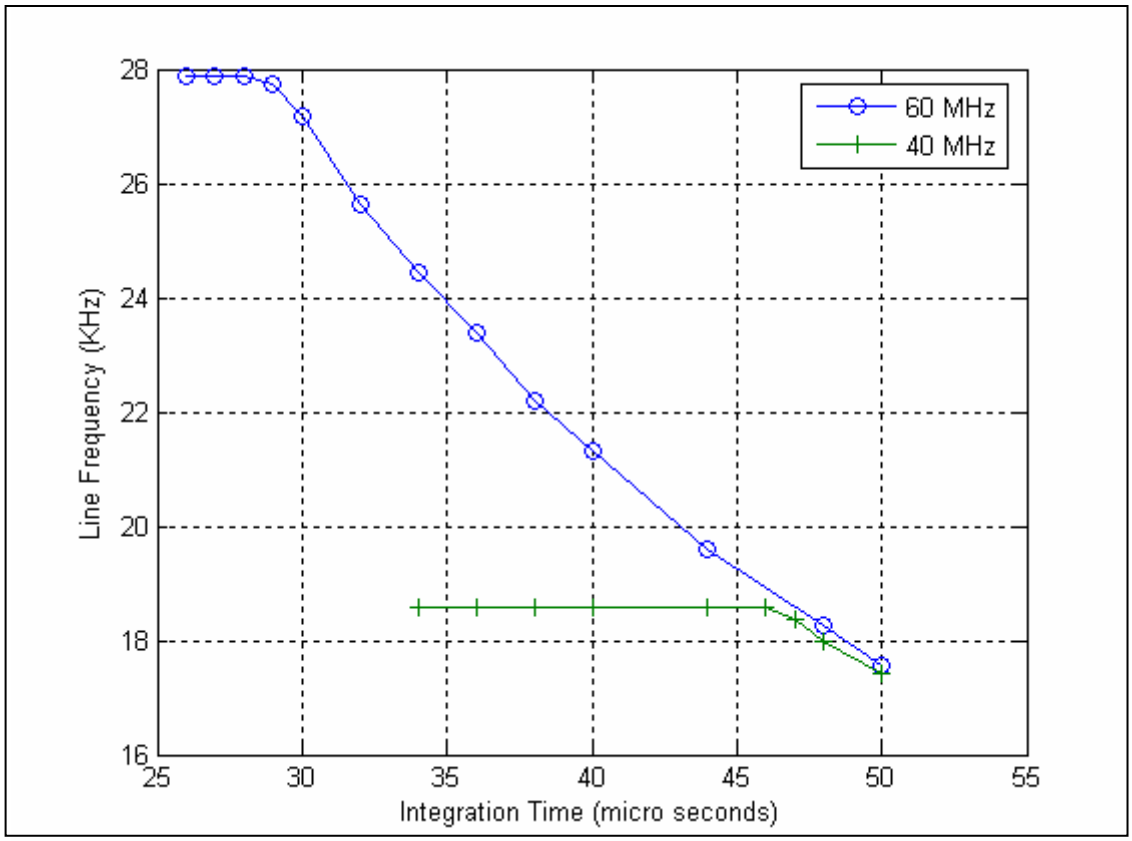


Figure A1: Line Frequency Versus Integration Time for line scan camera operating at 60MHz and 40MHz

# APPENDIX C

## SPECIFICATIONS OF LINE SCAN CAMERA

## Typical Performances

**Table 1.** Typical Performances

| Parameter | Value | | | | Unit |
|---|---|---|---|---|---|
| **Sensor Characteristics at Maximum Pixel Rate** | | | | | |
| Resolution | 512 | 1024 | 2048 | 4096 | pixels |
| Pixel size (square)<br><br>– | 14<br><br>– | 14<br><br>10 | 14<br><br>10 | –<br><br>10 | µm<br><br>µm |
| Max Line rate | 98 | 53 | 28 | 14 | kHz |
| Anti blooming | x 150 | | | | – |
| **Radiometric Performances (maximum Pixel Rate, Tamb = 25°C)** | | | | | |
| Output format | 12 (also configurable in 8 or 10) | | | | bit |
| Spectral range | 250 - 1100 | | | | nm |
| Linearity | < 1 | | | | % |
| Gain range<br>(step of 0.047 dB) | Gmin<br>0 | Gnom<br>18 | Gmax<br>30 | | dB |
| Peak response[1][2] with 14 µm pitch<br>10 µm pitch | 130<br>50 | 1040<br>400 | 4180<br>1600 | | LSB/(nJ/cm$^2$)<br>LSB/(nJ/cm$^2$) |
| SNR<br>Effective bit | 67.4<br>11.2 | 49<br>8.2 | 37<br>6.2 | | dB<br>bit |
| Input RMS Noise with 14 µm pitch<br>10 µm pitch | 14<br>37 | | | | pJ/cm$^2$<br>pJ/cm$^2$ |
| PRNU (Pixel Response Non Uniformity) | ± 3% (± 10% max) | | | | % |
| **Mechanical and Electrical Interface** | | | | | |
| Size (w x h x l) | 56 x 60 x 39.4 | | | | mm |
| Lens mount | C, F, T2, M42 x 1 | | | | – |
| Sensor alignment<br>(See "Sensor Alignment" on page 14) | $\Delta x,y = \pm 50 - \Delta z = \pm 30 - \Delta tilt_z = 0\text{-}35$<br>$\Delta \theta x,y = \pm 0.2$ | | | | µm<br>° |
| Power supply | DC, single 12 to 24V | | | | V |
| Power dissipation | < 7 | | | | W |
| Operating temperature[3] | 0 to 65 (non condensing) | | | | °C |
| Storage temperature | -40 to 75 (non condensing) | | | | °C |

Spectral Response

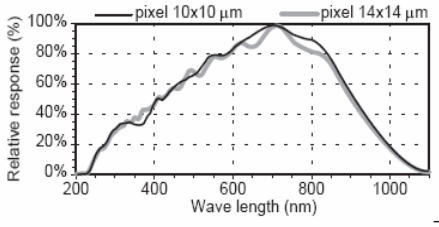


Notes: 1. LSB are given for 12-bit configuration
2. nJ/cm$^2$ measured on the sensor
3. Camera front face temperature

REFERENCES


[1] A F Fercher, W Drexler, C K Hitzenberger and T Lasser, “Optical coherence tomography - principles and applications,” Rep. Prog. Phys. 66 No (February 2003) 239-303.

[2] D. Huang , E. A. Swanson, C.P. Lin, J.S. Schuman, W. G. Stinson, W. Chang, M.R. Hee,T.Flotte, K Gregory,C.A. Puliafito, and J.G. Fujimoto, “Optical Coherence Tomography,” Science 254 1178 (1991).

[3] P H Tomlins and R K Wang “Theory, developments and applications of optical coherence tomography,” J. Phys. D: Appl. Phys. 38 No 15 (7 August 2005) 2519-2535.

[4] Joseph M. Schmitt “Optical Coherence Tomography (OCT): A Review,” IEEE J. of selected topics in quantum electronics, 5(4), (July/August 1999).

[5] M. R. Hee, J. A. Izatt, E. A. Swanson, D. Huang, J. S. Schuman, C. P. Lin, C. A. Puliafito, and J. G. Fujimoto, “Optical coherence tomography for ophthalmic imaging,” IEEE Engineering in Medicine and Biology, pp. 67-76, 1995.

[6] G. Häusler, “ Coherence radar and spectral radar -new tools for dermatological diagnosis,” J. Biomed. Opt., 3, 21-31, 1998.

[7] M.W. Lindner, P Andretzky, F Kiesewetter, and A. F. Fercher, “Spectral Radar:Optical Coherence Tomography in the Forier Domain,” Handbook of Optical Coherence Tomography (2002) Pages 335-357.

[8] Wojtkowski M, Leitgeb R, Kowalczyk A, Bajraszewski T, Fercher AF, “In vivo human retinal imaging by Fourier domain optical coherence tomography,” J Biomed Opt. 2002 Jul; 7(3):457-63.

[9] A. F. Fercher, C. K. Hitzenberger, G. Kamp and S. Y. El-Zaiat, “Measurement of intraocular distances by backscattering spectral Interferometry,” ARTICLE Optics Communications, Volume 117, Issues 1-2, 15 May 1995, Pages 43-48.

[10] Yuichi Teramura et al 2000 “Two-dimensional optical coherence tomography using spectral domain interferometry,” J. Opt. A: Pure Appl. Opt. 2 No 1 January 2000, Pages 21-26.

[11] N Nassif, B Cense , B H Park, M C Pierce, S H Yun , B E Bouma , G J Tearney, T C Chen and J F de Boer, "In vivo high-resolution video-rate spectral-domain optical coherence tomography of the human retina and optic nerve," Optics Express, vol. 12, Issue 3, p.367

[12] A. Rollins, S. Yazdanfar, M. Kulkarni, R. Ung-Arunyawee, and J. Izatt, "In vivo video rate optical coherence tomography," Opt. Express 3, 219-229 (1998)

[13] W. Drexler, U. Morgner, F. X. Krtner, C. Pitris, S. A. Boppart, X. D. Li, E. P. Ippen, and J. G. Fujimoto, "In-vivo ultrahigh-resolution optical coherence tomography," Optics Letters, Vol. 24 Issue 17 Page 1221 (September 1999).

[14] S. H. Yun, G. J. Tearney, B. E. Bouma, B. H. Park, J. F. de Boer, "High-speed spectral-domain optical coherence tomography at 1.3 μm wavelength," Optics Express, Vol. 11 Issue 26 Page 3598 (December 2003).

[15] Johannes F. de Boer, Barry Cense, B. Hyle Park, Mark C. Pierce, GuillermoJ. Tearney and Brett E. Bouma, "Improved signal-to-noise ratio in spectral-domain compared with time-domain optical coherence tomography," Optics Letters, Vol. 28 Issue 21 Page 2067 (November 2003).

[16] R. A. Leitgeb, C. K. Hitzenberger and A. F. Fercher, "Performance of fourier domain vs. time domain optical coherence tomography," Optics Express, Vol. 11 Issue 8 Page 889 (April 2003)

[17] A.V. Zvyagin, "Fourier-domain optical coherence tomography: optimization of signal-to-noise ratio in full space," Optics Communications, Volume 242, Issues 1-3, 26 November 2004, Pages 97-108

[18] J S Schuman, "Quantification of nerve fiber layer thickness in normal and glaucomatous eyes using optical coherence tomography," Arch. Ophthalmol. 113, 586–596 (1995).

[19] M R Hee, "Quantitative assessment of macular edema with optical coherence tomography,"Arch. Ophthalmol. 113, 1019–1029 (1995).

[20] A. Sergeev, V. Gelikonov, G. Gelikonov, F. Feldchtein, R. Kuranov, N. Gladkova, N. Shakhova, L. Snopova, A. Shakhov, I. Kuznetzova, A. Denisenko, V. Pochinko, Y. Chumakov, and O. Streltzova, "In vivo endoscopic OCT imaging of precancer and cancer states of human mucosa," Opt. Express 1, 432-440 (1997).

[21] K Kobayashi K, J A Izatt, M D Kulkarni, J Willis, and Jr. M V Sivak, "High-resolution cross-sectional imaging of the gastrointestinal tract using optical coherence tomography: preliminary results," Gastrointest. Endosc. 47, 515–523

[22] Andrew M. Rollins, Rujchai Ung-arunyawee, Amitabh Chak, C. K. Wong, Kenji Kobayashi, Michael V. Sivak Jr. and Joseph A. Izatt, “Real-time in vivo imaging of human gastrointestinal ultrastructure by use of endoscopic optical coherence tomography with a novel efficient interferometer design,” Optics Letters, Vol. 24, Issue 19, pp. 1358-1360 (October 1999).

[23] F. Feldchtein, G. Gelikonov, V. Gelikonov, R. Kuranov, A. Sergeev, N. Gladkova, A. Shakhov, N. Shakhova, L. Snopova, A. Terent'eva, E. Zagainova, Y. Chumakov, and I. Kuznetzova, “Endoscopic applications of optical coherence tomography,” Opt. Express 3, 257-270 (1998).

[24] P. R. Herz, Y. Chen, A. D. Aguirre, K. Schneider, P. Hsiung, J. G. Fujimoto, K. Madden, J. Schmitt, J. Goodnow, and C. Petersen, “Micromotor endoscope catheter for in vivo, ultrahigh-resolution optical coherence tomography,” Opt. Lett. 29, 2261-2263 (2004).

[25] Bahaa E.A.Saleh and Malvin Carl Teich, Fundamentals of Photonics, ISBN 0471839655.

[26] K B Langer, High resolution optical coherence tomography system for integration with a multimodal optical imaging workstation. Master’s Thesis. UT Arlington, May 2006.

[27] Christopher Palmer. Diffraction Grating Handbook, Fifth Edition. Thermo RGL

[28] C. Dorrer, “Influence of the calibration of the detector on spectral interferometry,” J. Opt. Soc. Am. B 16, 1160-1168 (1999).

[29] C. Dorrer, N. Belabas, J. P. Likforman, and M. Joffre, “Spectral resolution and sampling issues in Fourier-transform spectral interferometry,” J. Opt. Soc. Am. B 17, 1795-1802 (2000).

[30] Max Born and Emil Wolf et al., Principles of optics : electromagnetic theory of propagation, interference and diffraction of light ISBN: 0521642221.

[31] J. Zhang, J. S. Nelson, and Z. Chen, “Removal of a mirror image and enhancement of the signal-to-noise ratio in Fourier-domain optical coherence tomography using an electro-optic phase modulator,” Opt. Lett. 30, 147-149 (2005).

[32] J. Ai and L. V. Wang, “Synchronous self-elimination of autocorrelation interference in Fourier-domain optical coherence tomography,” Opt. Lett. 30, 2939-2941(2005).

[33] Nader Nassif, Barry Cense, B. Hyle Park, Seok H. Yun, Teresa C. Chen, Brett E. Bouma, Guillermo J. Tearney and Johannes F. de Boer, “In vivo human retinal imaging by ultrahigh-speed spectral domain optical coherence tomography,” Optics Letters, Vol. 29 Issue 5 Page 480 (March 2004).

[34] M. Wojtkowski, A. Kowalczyk, R. Leitgeb, A. F. Fercher, “Full range complex spectral optical coherence tomography technique in eye imaging,” Optics Letters, Vol. 27 Issue 16 Page 1415 (August 2002)

[35] Christoph K. Hitzenberger, Peter Trost, Pak-Wai Lo and Qienyuan Zhou, “Three-dimensional imaging of the human retina by high-speed optical coherence tomography,” Optics Express, Vol. 11 Issue 21 Page 2753 (October 2003).

[36] Shuliang Jiao, Robert Knighton, Xiangrun Huang, Giovanni Gregori andCarmen A. Puliafito, “Simultaneous acquisition of sectional and fundus ophthalmic images with spectral-domain optical coherence tomography,” Optics Express, Vol. 13 Issue 2 Page 444 (January 2005).

## BIOGRAPHICAL INFORMATION

Manish Kankaria was born on 20th December, 1978 in Raiganj -West Bengal, India. He completed his schooling from Bharatiya Vidya Bhavan, Kolkata, India and received his Bachelor's degree in Instrumentation and Electronics Engineering from Bangalore Institute of Technology, Bangalore, India in 2001. He served as Junior Research Assistant in microelectronics division of Indian Institute of Technology, Kharagpur, India for about a year.

In fall, 2003 he started his graduate studies in Joint Program of Biomedical Engineering at the University of Texas at Arlington and University of Texas Southwestern Medical Center at Dallas. He joined the biomedical optics lab as a Graduate Research Assistant and implemented a high speed Fourier-Domain Optical Coherence Tomography system.